2017

Axial load-bending moment diagrams of GFRP reinforced columns and GFRP encased square columns

Jim Youssef
University of Wollongong, jy201@uowmail.edu.au

Muhammad N. S Hadi
University of Wollongong, mhadi@uow.edu.au

Publication Details

Youssef, J. & Hadi, M. N. S. (2017). Axial load-bending moment diagrams of GFRP reinforced columns and GFRP encased square columns. Construction and Building Materials, 135 550-564.

Axial load-bending moment diagrams of GFRP reinforced columns and GFRP encased square columns

Abstract
Fiber reinforced polymer (FRP) pultruded materials are available in a wide variety of shapes, including bars, I-sections, C-sections and other structural sections. Due to their high durability, low self-weight and reduced maintenance costs, these FRP materials are becoming a competitive option for replacing steel as structural materials especially in corrosive environments. This paper summarizes an experimental program on the axial and flexural behaviour of square concrete members reinforced with glass fiber reinforced polymer (GFRP) bars and embedded with pultruded GFRP structural sections under different loading conditions. Furthermore, an analytical model is presented to predict the axial load-bending moment interaction diagrams of the experimentally tested specimens. It can be concluded from this study that the analytical models provide reliable estimates of the maximum load and bending moment capacities of GFRP reinforced and GFRP encased concrete columns. In addition, a parametric study was conducted to study the effects of concrete compressive strength and longitudinal GFRP reinforcement ratio on the structural performance of GFRP reinforced square concrete columns.

Keywords
square, columns, reinforced, gfrp, diagrams, moment, load-bending, axial, encased

Publication Details
Youssef, J. & Hadi, M. N. S. (2017). Axial load-bending moment diagrams of GFRP reinforced columns and GFRP encased square columns. Construction and Building Materials, 135 550-564.

Axial Load-Bending Moment Diagrams of GFRP Reinforced Columns and GFRP Encased Square Columns

Jim Youssef[1] and Muhammad N.S. Hadi [2]

Abstract

Fiber reinforced polymer (FRP) pultruded materials are available in a wide variety of shapes, including bars, I-sections, C-sections and other structural sections. Due to their high durability, low self-weight and reduced maintenance costs, these FRP materials are becoming a competitive option for replacing steel as structural materials especially in corrosive environments. This paper summarizes an experimental program on the axial and flexural behaviour of square concrete members reinforced with glass fiber reinforced polymer (GFRP) bars and embedded with pultruded GFRP structural sections under different loading conditions. Furthermore, an analytical model is presented to predict the axial load-bending moment interaction diagrams of the experimentally tested specimens. It can be concluded from this study that the analytical models provide reliable estimates of the maximum load and bending moment capacities of GFRP reinforced and GFRP encased concrete columns. In addition, a parametric study was conducted to study the effects of concrete compressive strength and longitudinal GFRP reinforcement ratio on the structural performance of GFRP reinforced square concrete columns.

Keywords: Square Concrete Columns; GFRP Reinforcement; Application of FRPs; Hybrid structures; Pultruded shapes; P-M Interaction Diagram

[1]Ph.D. Candidate, School of Civil, Mining and Environmental Engineering, University of Wollongong, Wollongong, NSW 2522, Australia. Email: jy201@uowmail.edu.au

[2]Associate Professor, School of Civil, Mining and Environmental Engineering, University of Wollongong, Wollongong, NSW 2522, Australia. Email: mhadi@uow.edu.au, *Corresponding Author

1.0 Introduction

The use of reinforcement with FRP composite materials have emerged as one of the alternatives to steel reinforcement for concrete structures prone to corrosion issues. Currently, design standards have been developed for FRP reinforced flexural members, including ACI 440.1R – 15 [1]. On the other hand, the level of understanding of the behaviour of FRP reinforced compression members has not reached a level where design standards are available for such members. Having said this, the current ACI 440.1R – 15 [1] design guideline mentions to neglect the compressive contribution of FRP reinforcement when used as reinforcement in columns, in compression members, or as compression reinforcement in flexural members. Therefore, the acceptance of FRP by designers requires the development of design guidelines for the design of FRP bars in compression members such as columns. In this regard, limited experimental and analytical studies have been conducted to understand the compressive behaviour and failure modes of concrete columns internally reinforced with FRP and subjected to different loading conditions as discussed herein.

Kawaguchi [2] conducted an experimental study of twelve concrete specimens reinforced with aramid fiber-reinforced polymer (AFRP) bars. The specimens were tested in eccentric compression or tension. This study reported that the AFRP reinforced columns can be analysed using the same approach undertaken for concrete columns reinforced with steel bars. Choo et al. [3] reported that unlike steel reinforced columns, FRP reinforced columns interaction diagrams do not experience balance points due to the linear elastic material properties of the FRP bars until failure. Furthermore, FRP reinforced columns have a tendency to exhibit a failure point before the strength interaction reaches a pure bending condition, which is classified as brittle-tension failure due to the tensile rupture of the FRP bars. They reported that this failure occurs when low reinforcement ratios are considered. Therefore, Choo et al. [4] presented a set of equations for rectangular columns subjected to

46 pure bending, to calculate the minimum FRP reinforcement ratio to prevent the tensile failure
47 of the FRP bars in the tension side. Zadeh and Nanni [5] developed interaction diagrams for
48 GFRP reinforced columns subjected to combined flexural and axial loads by assuming the
49 GFRP longitudinal bars are only effective in tension. Therefore, compression GFRP bars
50 were replaced by an equivalent area of concrete. Furthermore, the authors suggested
51 imposing a limit of 1% on the maximum design tensile strain of GFRP longitudinal bars in
52 order to avoid exaggerated deflections. In another study, Hadi et al. [6] tested circular
53 concrete columns reinforced with GFRP bars and helices under concentric and eccentric
54 loading conditions. The load carrying and bending moment capacities of the GFRP reinforced
55 specimens were calculated analytically with the same principles used for conventional steel
56 reinforced specimens and were compared with the experimental results.

57 The alternative use of FRP structural profiles and tubes in concrete members presents a very
58 interesting potential, either for rehabilitation of existing structures or for new construction
59 due to their many advantages including low self-weight, ease of installation, low maintenance
60 costs and corrosion resistance. However, FRP profiles generally have low in-plane moduli
61 and wall slenderness making them particularly vulnerable to local buckling. Tomblin and
62 Barbero [7] reported that the strength of short columns made of GFRP I-sections are
63 governed by local buckling, while Zureick and Scott [8] concluded that the failure
64 mechanism of long columns is by global buckling. There have been several studies aimed to
65 examine the structural advantages of connecting GFRP pultruded profiles to concrete
66 compression and flexural elements to make better use of the profiles [9.10]. However, the
67 encasement of GFRP structural sections in concrete columns has only been studied by Hadi
68 and Youssef [11].

69 This study is a continuation of the experimental study of Hadi and Youssef [11] in which an
70 experimental program investigating the behaviour of GFRP reinforced and GFRP encased

71 concrete columns and beams was presented. Parameters investigated included the magnitude
72 of load eccentricity and type of internal reinforcement with steel reinforced, GFRP
73 reinforced, GFRP I-section encased and GFRP C-sections encased concrete specimens tested
74 under compressive and flexural loading. This paper presents an analytical model to predict
75 the load-interaction diagrams of GFRP reinforced and GFRP encased square concrete
76 specimens and attempts to theoretically validate the experimental results of Hadi and Youssef
77 [11].

78 **2.0 Experimental Program**

79 *2.1. Design of Specimens*

80 The experimental component of this study involved testing four groups of four square
81 reinforced concrete columns under concentric as well as combined axial and flexural loading.
82 The first group of specimens were reinforced with steel bars (Group RS) and the second
83 group of specimens were reinforced with GFRP bars (Group RF). The first two groups of
84 specimens were designed to have similar longitudinal and transverse reinforcement ratios.
85 The longitudinal reinforcement ratio of the Group RS and Group RF specimens were 1.03
86 and 1.15%, respectively. The third (Group I) and fourth group (Group C) of specimens were
87 encased with a pultruded GFRP I-section and C-sections, respectively. Each specimen had a
88 square cross section with a side dimension of 210 mm and a height of 800 mm. The
89 reinforcement details of all the groups of specimens are shown in Figure 1. Each group
90 consisted of four specimens; one specimen was tested concentrically, one tested under 25 mm
91 eccentricity, one tested under 50 mm eccentricity and the last specimen was tested as a beam
92 under four point loading test. The specimens are identified by the type of internal
93 reinforcement and magnitude of load eccentricity. For example, Specimen RS-25 is

reinforced with steel bars and is eccentrically loaded at 25 mm from the centreline. The letter "B" denotes a beam specimen tested under flexural loading.

A detailed discussion of the design, preparation, testing and instrumentation of the specimens is discussed in Hadi and Youssef [11].

2.2 Preliminary Testing

In this study, all the concrete specimens were cast on the same day. The average compressive strength of the concrete (f_c') at 28 days was determined to be 29.3 MPa. Furthermore, the average compressive strength of concrete at the first day and last day of testing the specimens was 31 MPa and 35.3 MPa, respectively. The compressive strengths were obtained by testing cylinders having a diameter of 100 mm and height of 200 mm, with five cylinders tested for each the 28 day and last day of testing and three cylinders tested on the first day of testing to obtain an average value for each day of testing.

Deformed steel N12 bars were used as longitudinal reinforcement in Group RS specimens. Five samples were tested in accordance with AS 1391- 2007 [12] to determine the tensile properties of the reinforcing steel bars. The average yield stress (f_{sy}), yield strain (ε_{sy}) and modulus of elasticity (E_s) were determined to be 540 MPa, 0.324% and 200 GPa, respectively. Sand coated No. 4 (#4) GFRP bars of 12.7 mm standard diameter were used to reinforce the Group RF specimens longitudinally. The GFRP bars were manufactured by Pultrall Inc. [13]. Five samples were tested in accordance with ASTM D7205-11 [14] to determine the tensile properties of the GFRP bars. The ultimate tensile stress, corresponding rupture strain and tensile modulus of elasticity were 1641 MPa, 2.41% and 67.9 GPa, respectively. These properties were calculated based on the bar's standard diameter of 12.7 mm which was provided by the manufacturer [13].

GFRP pultruded I-sections and C-sections were used in the specimens of Group I and C, respectively and they were supplied by GRP Australia [15]. The tensile properties of the GFRP pultruded sections were determined based on the test method ISO 527-4-1997 [16] and are shown in Table 1. Five coupon samples from each GFRP C-section, web of the I-section and flange of the I-section were extracted in the longitudinal direction using a wet saw machine. The coupons had nominal dimensions of 300 mm long and 25 mm wide and were tested using a screw-driven material testing machine known as the 500 kN Instron 8033 machine. The compressive properties of the GFRP pultruded sections were determined based on the test method of ASTM D695-15 [17], as shown in Table 1. A total of 17 coupon samples from each web of the GFRP C-section, web of the I-section and flange of the I-section with nominal dimensions of 9.5 x 12.7 x 37.6 mm were extracted in the longitudinal direction using a wet saw machine from the sections. To compensate for levelling errors, either the top and bottom ends of the coupons were levelled with a mill and/or the coupons were placed on a spherical seat. The coupons were tested under compression by direct end loading using the Instron 8033 machine, as shown in Figure 2. Nine samples from the C-section and eight samples each from the web and flange of the I-section were instrumented with strain gauges to measure the elastic modulus in compression.

It can be concluded from the compression testing of the GFRP sections that there was a high dispersion in the results [11]. Most notably the coefficients of variation (COV) for the longitudinal compressive strength for the I-section and C-section were 15.5 and 26.9%, respectively. This dispersion in results may be the result of different issues such as premature failures due to geometric instabilities or local end crushing, poor quality control at the manufacturing level, the intrinsic nature of the test setup or due to the non-uniform placement of the fibers throughout the cross section. It should be noted that it has been reported that the compression testing of pultruded samples is difficult due to the high longitudinal strength and

low transverse strength of the material [18]. As a result, the ends of most of the coupons failed by either crushing or brooming. Therefore, the property measured may not be the actual compressive strength but represent the composite bearing strength [18]. In addition, from material testing it can be seen that the two shapes of GFRP sections varied in tensile and compressive properties. The web of the I-section also had slightly lower tensile and compressive strength and modulus as compared to the flange, as shown in Table 1.

3.0 Experimental Results

A detailed discussion of the strength, failure modes, failure locations and ductility of each group of specimens under different types of eccentric loading were analysed and addressed in Hadi and Youssef [11]. The following outlines the general behaviour and results of the tested column and beam specimens. The summary of the specimen testing results is shown in Table 2. For the eccentrically loaded column specimens (25 mm and 50 mm), the bending moment capacities (M_{exp}) corresponding to the first maximum axial load (P_{max}) was calculated by Eq. (1). It should be noted that P_{max} corresponds to the first maximum load before the total onset of concrete spalling after the initial linear region of the axial load – displacement curves. When calculating the bending moments, both the application of the load at an eccentricity (e) and secondary moments arising from the lateral deflection of the column at P_{max} (δ) were taken into account. For the beam specimens loaded under four-point loading, the bending moment capacity was calculated by Eq. (2). This equation was obtained from simple statics as the bending moment value between the two point loads as equalling half the maximum applied load on the beam specimens multiplied by the shear span length (a = 235 mm in this study).

The effects of eccentricity on the structural behaviour of the column specimens are shown in Figure 3. For all the groups of specimens, there was a reduction in the axial load carrying

166 capacity with an increase in load eccentricity. Furthermore, the GFRP encased specimens
167 failed at lower axial displacements as compared to the other specimens.

$$M_{exp} = P_{max}(e + \delta) \quad (1)$$

$$M_{exp} = \frac{P_{max}}{2} a \quad (2)$$

168 Strain gauges were also bonded on the internal longitudinal reinforcements and imbedded
169 sections. The location of the attached strain gauges is shown in Figure 1. For each
170 concentrically loaded specimen, two strain gauges were bonded to the longitudinal
171 reinforcement and imbedded sections at mid-height. Similarly, for the eccentrically loaded
172 specimens, two strain gauges were bonded on to the longitudinal bars, with one strain gauge
173 on the compression side and one on the tension side. For the imbedded GFRP I-sections, the
174 strain gauges were bonded in the middle of the two outside flanges at the mid-height. Only
175 one GFRP C-section per specimen was instrumented with strain gauges which were located
176 on the two flanges at mid-height, as shown in Figure 1.

177 At the first maximum load the average axial strain in the bars and GFRP sections for
178 Specimens RS-0, RF-0, I-0 and C-0 ranged between 0.35 to 0.40%. At this point the steel had
179 reached its yield point and the axial strain for the GFRP bars in Specimen RF-0 was 14.7% of
180 the ultimate tensile rupture strain. Similarly, for all the eccentrically loaded specimens the
181 strains in the instrumented compression reinforcement and sections ranged between 0.35 to
182 0.40% at the first maximum load. On the other hand, the strain in the reinforcement located in
183 the tensile zone of the eccentrically loaded specimens varied. At maximum load, the steel bar
184 in the tension zone was still under slight compression for Specimen RS-25, while the
185 instrumented reinforcement and sections for Specimens RF-25, I-25 and C-25 were under
186 slight tension with values ranging from 0.01% to 0.06%. However, the tensile reinforcement

and sections for the specimens loaded under 50 mm eccentric load were exposed to higher tensile strains at maximum load with values ranging from 0.08% to 0.19%. As mentioned above for the eccentrically loaded specimens only one strain gauge was placed on the tension and compression longitudinal bars and sections and no average could be obtained for each.

4.0 Analytical Modelling

4.1 Theoretical Considerations of Material Properties

This section describes the stress-strain relationship of the constituent materials used in this study. These materials include the concrete, steel reinforcement and GFRP reinforcement. The relationships and the experimental material properties are used to theoretically calculate the prediction of the bending moment and corresponding load carrying capacities of the eccentrically loaded concrete specimens.

4.1.1. Concrete

The stress-strain model proposed by Yang et al. [19] was used to develop the compressive stress of the unconfined concrete in terms of the strains as follows:

$$f_c = \left[\frac{(\beta_1 + 1)\left(\frac{\varepsilon_c}{\varepsilon_{co}}\right)}{\left(\frac{\varepsilon_c}{\varepsilon_{co}}\right)^{\beta_1+1} + \beta_1}\right] f_{co} \tag{3}$$

where f_c is the compressive stress corresponding to the compressive strain ε_c; f_{co} is the unconfined concrete strength which is equal to 85% of the compressive cylinder strength of concrete at the first day of testing; ε_{co} is the strain corresponding to f_{co}; and β_1 is a parameter that determines the slopes of the ascending and descending branches as illustrated below. It should be noted that a factor of 85% of the compressive cylinder strength of concrete is used in this study in order to take into account the size effect of the large concrete

207 specimens as compared to the small cylinders used to develop the stress-strain model. A
208 factor of 90% has also been investigated in the analysis as shown below in the later sections.

209 The parameter $\beta_1$controls the slope of the ascending and descending branch of the stress-
210 strain relationship, with Eq. (4) is used for the ascending branch and Eq. (5) is used for the
211 descending branch.

$$\beta_1 = 0.2exp(0.73\xi) \quad \text{for } \varepsilon_c \leq \varepsilon_0 \tag{4}$$

$$\beta_1 = 0.41exp(0.77\xi) \quad \text{for } \varepsilon_c > \varepsilon_0 \tag{5}$$

$$\xi = \left(\frac{f_{co}}{f_0}\right)^{0.67} \left(\frac{w_0}{w_c}\right)^{1.17} \tag{6}$$

212 where f_o and w_o are reference values equal to 10 MPa and 2300 kg/m^3, respectively; and w_c is
213 the concrete density assumed to be 2400 kg / m^3 for normal-weight concrete.

214 The modulus of elasticity (E_c) is calculated using Eq. (7) as proposed in AS3600 – 2009 [20]
215 for concrete strengths less than 40 MPa. The unconfined concrete strain (ε_{co}) corresponding
216 to f_{co} is calculated using Eq. (8) as proposed by Yang et al. [19].

$$E_c = \left(0.043\sqrt{f_{co}}\right)(w_c)^{1.5} \tag{7}$$

$$\varepsilon_{co} = 0.0016exp\left[240\left(\frac{f_{co}}{E_c}\right)\right] \tag{8}$$

217 As noted above, the average compressive strength of concrete at 28 days, the first day and
218 last day of testing the specimens was 29.3, 31 MPa and 35.3 MPa respectively. Therefore,
219 herein the strength of each specimen in the analytical model was calculated using the
220 concrete compressive strength at the first day of testing of 31 MPa.

4.1.2. Steel Longitudinal Bars

The stress-strain relationship of the experimentally tested N12 bars is shown in Figure 4a. For simplicity, in the analytical study the stress-strain relationship of the longitudinal steel reinforcing bars is idealised to exhibit a bilinear elasto—plastic behaviour for both tension and compression as shown in Figure 4b. In the linear elastic region, the tensile strain in the steel does not reach the yield stress and the stress of the steel reinforcement is determined as follows:

$$f_s = \varepsilon_s E_s \tag{7}$$

where f_s is the tensile stress and E_s is the modulus of elasticity of the steel reinforcements.

On the other hand, in the post yield stage, the steel reinforcement reaches yield such that the stress is equal to the yield tensile stress (f_{sy}), as follows:

$$f_s = f_{sy} \tag{8}$$

4.1.3. GFRP Longitudinal Bars

The GFRP reinforcing bars behave in a linear brittle manner up to failure when loaded in tension. In this study, the actual stress-strain response of the GFRP bars obtained by tensile testing illustrates the idealised linear elastic behaviour, as shown in Figure 5.

When loaded in compression, the behaviour of FRP bars is influenced by different modes of failure including transverse tensile failure, fiber microbuckling, or shear failure [1]. Therefore, there is no standard axial compression test method for FRP composites. However, the behaviour of FRP bars in compression needs to be established to allow for the design of FRP reinforced concrete columns. It has been reported that the compressive strengths of FRP bars are relatively low compared to the tensile strengths. In early studies, the compressive strengths of GFRP bars were reported to be 55% of the tensile strengths, while the compressive modulus of elasticity were 80% of the tensile modulus of elasticity [21-23].

243 Chaallal and Benmokrane [24] showed that the compressive strength of GFRP rods were
244 77% of the tensile strength. Kobayashi and Fujisaki [25] found that the compressive
245 strengths of the GFRP bars were 30 to 40% of their tensile strengths. Deitz et al. [26]
246 reported that the ultimate compressive strength is approximately equal to 50% of the ultimate
247 tensile strength, whereas there was no difference in the modulus of elasticity in compression
248 compared to that in tension. These studies indicate the test data of compression testing of
249 GFRP bars are widely scattered and subjected to significant variations, unlike the tensile
250 properties. Taking this into account, the compressive properties used in the analytical study
251 are explained in the sections below.

252 Considering the linear brittle behaviour of GFRP bars, the tensile stress in each bar can be
253 calculated using Hooke's Law, as follows:

$$f_{ft} = \varepsilon_{ft} E_{ft} \tag{9}$$

254 where f_{ft} is the tensile stress and E_{ft} is the tensile modulus of GFRP longitudinal
255 reinforcements.

256 Similarly, the compressive stress in each bar can be calculated using Hooke's Law, as
257 follows:

$$f_{fc} = \varepsilon_{fc} E_{fc} \tag{10}$$

258 where E_{fc} is the compressive modulus of GFRP longitudinal reinforcements.

259 *4.1.4. GFRP Pultruded Sections*

260 GFRP pultruded sections are orthotropic materials with the fibers laid mainly in the
261 longitudinal direction. Therefore, these sections are stronger in the longitudinal direction as
262 compared with the transverse direction. The sections are usually too narrow in the transverse
263 direction to enable the extraction of standard coupons with dimensions as specified by the test
264 standards. Therefore, the transverse tensile properties of the pultruded structural sections

could not be determined. Furthermore, considering the loads on columns are in the longitudinal direction, only the longitudinal properties will be used in the analytical study.

Similar to GFRP bars the GFRP pultruded sections are linear elastic materials in both tension and compression. Therefore, the tensile and compressive stresses can be calculated from Hooke's Law similar to that of Eqs. (9) and (10), respectively.

4.2. Load Capacity of Concentrically Loaded Column Specimens

4.2.1. Steel Reinforced Specimens (Group RS)

When a column is subjected to a concentric load (e = 0), the column shortens uniformly with increasing load. The longitudinal strains in the steel reinforcement and concrete are equal at all stages of loading [27]. ACI 318-14 [27] uses the following equation to represent the axial load capacity of conventional steel reinforced concrete columns under concentric loading:

$$P_o = 0.85 f_c (A_g - A_{st}) + f_{sy} A_{st} \tag{11}$$

where f_c is the concrete compressive strength; A_g is the gross sectional area of concrete; A_{st} is the total area of longitudinal reinforcement; and f_{sy} is the yield strength of the longitudinal reinforcement.

For Specimen RS-0, the predicted axial load capacity using Eq. (11) and the concrete strength at the first day of testing (f_c = 31 MPa) is 1394 kN. Therefore, the ratio of the experimental axial capacity to the predicted value is 0.968. Some possible reasons for the theoretical capacity being slightly higher than the experimental value may be due to misalignment in the reinforcement or due to the variation in concrete strength.

4.2.2. GFRP Reinforced Specimens (Group RF)

The current American guide, ACI 440.1R-15 [1] states the contribution of FRP bars should be neglected when used as reinforcement in columns. Similarly, the Canadian standard, CSA S806-12 [28] allows the use of FRP bars as longitudinal reinforcement in axially loaded

columns only, but ignores the compressive contribution of the FRP bars when calculating the ultimate axial capacity, as shown in Eq. (12).

$$P_o = \alpha_1 f_c\left(A_g - A_f\right) \tag{12}$$

where $\alpha_1 = 0.85 - 0.0015 f_c \geq 0.67$; and A_f is the total cross-sectional area of the longitudinal GFRP bars.

Based on the literature, other equations have been developed to predict the nominal axial capacity of the GFRP reinforced concrete specimen. Tobbi et al. [29] showed that ignoring the compressive contribution of the GFRP bars in Eq. (12) underestimates the maximum axial capacity. Therefore, the compressive contribution of the GFRP bars to the overall column capacity was taken into account. This was done by considering the GFRP bars compressive contribution to be 35% of the tensile strength as suggested by Kobayashi and Fujisaki [25], as shown in Eq. (13).

$$P_o = 0.85 f_c\left(A_g - A_f\right) + 0.35 f_{ftu} A_f \tag{13}$$

where f_{ftu} is the tensile strength of the longitudinal GFRP bars

Tobbi et al. [30] proposed the most recent equation to calculate the nominal axial capacity, which also takes into account the compressive contribution of the GFRP longitudinal bars. In this equation, the compressive contribution of the GFRP longitudinal bars is calculated based on the elastic theory and from the material properties as shown in Eq. (14).

$$P_o = 0.85 f_c\left(A_g - A_f\right) + \varepsilon_o E_f A_f \tag{14}$$

where ε_o is the concrete strain at peak stress which is equal to 0.003 as defined by ACI 318-14 [27]; and E_f is the modulus of elasticity of the GFRP longitudinal reinforcement.

The ratios of the experimental axial capacity for the concentrically loaded column specimen reinforced with GFRP bars (Specimen RF-0) as compared to the theoretical values obtained

from Equations 12, 13 and 14 are shown in Table 3. It should be noted that the cross-sectional area used in the calculations was determined on the GFRP bar's standard diameter of 12.7 mm rather than by a value obtained from Immersion testing. Also the concrete strength at the first day of testing was used in the formulas. Furthermore, it was assumed that the compressive modulus was equal to the tension modulus as reported by Deitz et al. [26].

It can be seen that ignoring the contribution of the GFRP bars in Eq. (12) results in an underestimation of the maximum capacity of 18.3%. Furthermore, the ratio of the experimental maximum load to the predicted value using Eq. (13) is below one with a value of 0.892. This value indicates that this equation over estimates the nominal axial capacity of Specimen RF-0. On the other hand, Eq. (14) provides an under estimation of the maximum capacity of 2.6%. Therefore, Eq. (14) provided the most accurate estimate of the maximum capacity and will be used in this study for the GFRP reinforced and GFRP encased specimens.

4.2.3. GFRP Encased Specimens (Group I and C)

In this study, the same formula proposed by Tobbi et al. [30] is used to predict the axial capacity of the GFRP encased specimens with the assumption that the strain in the GFRP sections is approximately equal to the concrete ultimate strain, as shown in Eq. (14). The compressive modulus of elasticity was used in the calculations with the total average values from the web and flanges of the I-section adopted for those specimens (Global value in Table 1). For the C-sections, compression testing of only the webs was performed and hence the compression modulus of elasticity of such was adopted in calculating the axial capacity for Group C specimens. Furthermore, the actual measured dimensions of the cross-sections were slightly smaller than the nominal dimensions provided by the manufacturer. Therefore, the measured dimensions were used to determine the cross-sectional areas.

The ratios of the experimental axial capacity for the concentrically loaded specimen reinforced with GFRP sections (Specimens I-0 and C-0) as compared to the theoretical values obtained from Eq. (14) are shown in Table 4. It can be seen that there is a reasonable and accurate agreement between the experimental and calculated load capacity for these columns, especially for Specimen C-0.

4.3 Theoretical P-M Interaction Diagrams

An analytical axial load-bending moment (P-M) interaction diagram was plotted to represent the axial load (P) and corresponding bending moment (M) of each of the specimens. A number of assumptions consistent with those applicable to steel reinforced cross sections were used in the analysis to develop the theoretical P-M interaction diagrams of GFRP reinforced and GFRP encased concrete cross-sections. These assumptions are as follows:

- The distribution of strain is assumed to be linear along the height of the section or in other words plane sections remain plane after deformation.
- Strain compatibility exists between the constituent materials, i.e. concrete, steel and GFRP reinforcement and sections, such that a perfect bond is assumed amongst these materials
- In tension, concrete is weak and therefore its tensile strength is ignored
- The steel reinforcing bars behave as an elastic-perfectly plastic material in both tension and compression as shown in Figure 4.
- The GFRP reinforcing bars and GFRP pultruded sections behave as a linear brittle material with orthotropic properties, as shown in Figure 5.
- For the GFRP pultruded sections, only the flanges in compression and flanges in tension is assumed to contribute to the compressive and tensile resistance, respectively. In other words, the compressive and tensile resistance of the web of both the I-sections and C-sections is neglected. Furthermore, only the longitudinal tensile

and compressive properties were used in the analysis with the transverse properties ignored.

- The confinement effect of the lateral steel and GFRP stirrups is ignored.
- The stress-strain model of Yang et al. [19] for unconfined concrete in compression is adopted as defined in 'Material Properties and Theoretical Considerations' above.
- Considering the column specimens are considered as short specimens, the effects of slenderness was not taken into account when determining the theoretical P-M interaction relationships.

For calculation of the axial load capacities and moment capacities under eccentric loads and pure bending, two methods were analysed. The first method is the conventional rectangular stress block method to construct the interaction diagrams of steel RC columns following the Australian Standard AS3600 – 2009 [20]. The second method is the small strips concrete method as described by Yazici and Hadi [31]. What varies in the two methods is the approach to determining the concrete response in compression.

In the rectangular stress block method, the concrete compressive stresses are assumed to be uniform along the cross section along a depth of γd_n as shown in Figure 6, with the compressive force in the concrete determined by Eq. (15) for specimens of Group RS and RF. The rectangular stress block method was not implemented for specimens of Group I and C.

$$C_{c1} = \alpha_2 f_c b \gamma d_n \tag{15}$$

where, f_c is the concrete compressive strength on the first day of testing (31 MPa); d_n is the neutral axis depth from the top of the section; $\alpha_2 = 1.0 - 0.003 f_c$ within the limits $0.67 \leq \alpha_2 \leq 0.85$; and $\gamma = 1.05 - 0.007 f_c$ within the limits $0.67 \leq \gamma \leq 0.85$.

On the other hand, in the small strips method the concrete cross section is assumed to consist of small finite parallel strips with a thickness (t) of 1 mm and a width equal to the cross section width (b) of 210 mm, as shown in Figure 7. The number of strips (n) is equal to the depth of the cross section of 210 mm divided by the thickness of each strip. Therefore, the cross section was divided into 210 small strips. Based on the assumption that strain distribution is linear along the height of the section after bending, the strain in the centre of each strip ($\varepsilon_{c,n}$) can be calculated, by assuming the extreme concrete compressive fiber has reached the ultimate compressive strain of 0.003 as shown in Eq. (16). After calculating the strain in each concrete strip, the corresponding stress value ($f_{c,n}$) on the centre of each strip is calculated according to the stress-strain model for unconfined concrete explained above. With the basic assumption that the tensile strength of concrete is ignored in the calculations, the stresses corresponding to tensile strains (i.e. $\varepsilon_{c,n} < 0$) are assumed to be zero. After determining the stresses, the force reaction in the centre of each concrete strip ($C_{c,n}$) is calculated from Eq. (17) for specimens of Group RS and RF and from Eq. (18) for specimens of Group I and C. The difference in these two formulas will be explained below. The moment created by the force on each strip is calculated as the force in each strip multiplied by the distance to the centreline of the section as shown in Eq. (19). Therefore, the overall response of the concrete section is calculated as the summation of the forces acting on the strips, as shown in Eq. (20). In addition, the overall moment response of the concrete section is calculated as the summation of the moments with respect to the centreline of the section.

$$\varepsilon_{c,n} = 0.003 \times \frac{d_n - (n - \frac{1}{2})}{d_n} \tag{16}$$

$$C_{c,n}(Specimens\ RS\ \&\ RF) = f_{c,n} \times A_{c,strip} \tag{17}$$

$$C_{c,n}(Specimens\ I\ \&\ C) = f_{c,n} \times (A_{c,strip} - A_{GFRP,n}) \quad (18)$$

$$M_{c,n} = C_{c,n}\left[\frac{D}{2} - \left(n - \frac{1}{2}\right)\right] \quad (19)$$

$$C_{c,2} = \sum_{n=1}^{210} C_{c,n} \quad (20)$$

where, n = 1, 2, 3,….., 210th strip starting from the top of the section; $A_{c.strip}$ is the gross concrete cross sectional area for each strip ($b \times t$); and $A_{GFRP,n}$ is the area of the GFRP sections in the nth strip.

In both these methods the same approach is taken to find the stresses and forces in the tensile and compressive reinforcement. First the strains in the tensile and compressive reinforcement or flanges of the GFRP sections are calculated using similar triangles with the assumptions of linear strain distribution and the strain in the extreme concrete compressive fibre has reached the ultimate compressive strain of 0.003. The tensile strains are considered negative while the compressive strains are positive. The stress in each layer of reinforcement or flanges of the sections is then calculated by applying the stress-strain relationships for the constitutive materials (see Section 4.1). The forces in the reinforcement are calculated as the stresses multiplied by the area. However, it is important to note that the compressive response of the concrete using Eq. (15) and Eq. (17) for Specimens RS and RF does not take into account the existence of the compression reinforcement (top layer of bars) occupied in the concrete compression zone. Therefore, to take into account the compression reinforcement in the calculations, the force in the compression reinforcement is calculated using Eq. (21) and (22) such that if the top layer of bars is within the concrete compression zone, it is necessary to subtract 0.85f_c multiplied by the cross-sectional area of the bars in the top layer from the total force contribution of those bars. Both Eq. (21) and Eq. (22) are for the rectangular stress

417 block method. The same equations exist for the small strips method but the concrete
418 compression zone occupies a height of d_n instead of γd_n. Furthermore, for the bottom layer of
419 reinforcement these equations were not applied and the force in that layer was simply
420 calculated as the stress in that layer multiplied by the area even if that layer of bars occupied
421 the concrete compression zone. On the other hand, a slightly different approach was taken for
422 specimens of Group I and C to take into account the existence of the GFRP sections ($A_{GFRP,c}$)
423 occupied in the concrete compression zone for the small strips method. This was done by
424 subtracting the area of the GFRP sections, including flanges and also the webs, located in
425 each concrete strip in the compression zone as shown in Eq (18). The forces for either the top
426 or bottom flanges for Group I and C specimens were simply calculated as the area of the
427 flanges (shaded regions in Figure 8) multiplied by the stresses in the flanges with positive
428 force denoting compression and negative force implying tension. As mentioned above, the
429 force contribution of the webs were neglected. It is important to note that the rectangular
430 stress block was not used for specimens of Groups I and C as it was quite complex to take
431 into account the areas of the GFRP sections located in the concrete compression block and
432 the corresponding lever arms and hence only the small strips method was utilised for these
433 specimens considering each concrete layer is analysed separately instead of one whole block.

If $\gamma d_n < d_{co}$: $$C = f_{comp} A_{comp} \quad (21)$$

If $\gamma d_n > d_{co}$: $$C = f_{comp} A_{comp} - 0.85 f_c A_{comp} \quad (22)$$

434 where, d_{co} is the distance from the top of the section to the centre of the top layer of
435 reinforcement; and f_c is the concrete compressive cylinder strength at the first day of testing.

436 Therefore, using the two methods the axial load carrying capacity is equal to the summation
437 of forces acting on the reinforcement, forces acting on the flanges of the GFRP encased
438 sections and the forces acting on the concrete compressive section. Similarly, the moment

carrying capacity is equal to sum of the moments with respect to the centreline of the section under a given eccentricity. The applied eccentricity is equal to the bending moment capacity divided by the axial load capacity.

The theoretical load-moment interaction diagrams for each method were drawn based on twelve data points. The first point represents the axial load capacity of the specimens under concentric loading with no applied eccentricity. The axial capacity for all the groups of specimens loaded concentrically were as explained in the above section of 'Load Capacity of Concentrically Loaded Column Specimens'. The rest of the points represent the axial load and bending moment capacity specimens loaded with a combined axial load and bending moment with the second point expressing the data point of the 25 mm eccentric loaded specimen. The rest of the data points are obtained with gradually increasing the eccentricity up until the pure bending condition. The process is as follows.

Using the goal seek function in Excel, the applied eccentricity is set to the required value by changing only the neutral axis depth value (d_n). The eccentricity is calculated as the moment capacity divided by the load capacity. The goal seek function determines the corresponding strains, stresses and force components acting in the reinforcement and concrete strips or blocks and subsequently determines the respective axial and bending moment capacities to obtain the set chosen value of eccentricity, by only changing the neutral axis depth input. This process is repeated by varying the eccentricity value to obtain the data points on the load-moment interaction diagram up until the pure bending condition. As mentioned above, the compressive strength at the first day of testing was used to develop the theoretical P-M interaction diagrams. Simply using the 28 day cylinder compressive strength of concrete would underestimate the theoretical P-M interaction diagrams.

5.0 Analytical versus Experimental Results

Plotting an experimental P-M diagram based on four points of loading would not accurately predict the load and bending moment capacities especially when all the loading points are not identified, most notably the balanced points. Therefore, the first maximum load (P_{max}) and corresponding bending moment capacities (M_{exp}) of the experimentally tested specimens, as shown in Table 2, were plotted as points on the theoretical P-M interaction diagrams.

Although the eccentrically loaded GFRP reinforced and GFRP encased specimens were able to sustain a slight increase in load after P_{max} [11], the eventual failure after this second peak load (P_{peak}) was brittle and explosive with no warning signs with failure occurring at or not long after this load, as shown in Figure 3 [11]. As a result, the analytical axial load-bending moment diagrams were drawn for the GFRP reinforced and encased specimens corresponding to the first maximum load (P_{max}) before the activation of the confinement effect of the stirrups and thus just before the onset of concrete spalling. Therefore, the confinement effect of the lateral steel and GFRP stirrups is ignored and an unconfined concrete model was adopted in the analysis.

The theoretical P-M interaction diagrams and the experimental results for all the groups of specimens are shown in Figures 9 – 12. For comparison purposes, the theoretical load and bending moment capacities for the 25 mm and 50 mm eccentrically loaded specimens were plotted as circular data points on the P-M diagram, in order to compare the same values obtained experimentally which were denoted by the square data points. It should be noted that the results of the GFRP reinforced and GFRP encased beam specimens were not presented and plotted against the theoretical P-M diagrams as the failure of these beam specimens prepared were in shear or bearing rather than in flexure and there were inconsistencies in the testing of these specimens as discussed in Hadi and Youssef [11]. In addition, the experimental results of the GFRP reinforced beam specimen could not be

compared to the theoretical models. Further research elaboration is necessary to investigate the beams by taking into account ACI 440.1R – 15 [1] provides guidelines for the flexure design of FRP reinforced beams designed to be controlled by either concrete crushing or FRP rupture.

The experimental load and moment capacities of the steel reinforced specimens (Group RS) for all loading types were close to the theoretical P-M diagrams for both methods, as shown in Figure 9. All the experimental data points except for the pure compression point lied above the P-M diagram using the small strips method. However, for the rectangular stress block P-M diagram, the data point of the 25 mm eccentric loaded specimen was slightly under the P-M interaction diagram, with the theoretical load capacity being 3.9% greater than the experimental load capacity. Some possible reasons for the theoretical load capacity of this data point being slightly higher than the experimental value may be due to either misalignment in the reinforcement or variation in concrete strength or specimen alignment errors. Therefore, the P-M diagram developed from the small strips method provided a more conservative estimate of the load and bending moment capacities as compared to the rectangular stress block. In general, both the developed theoretical models yielded results that are comparable to the experimental results for Group RS specimens.

For the GFRP reinforced specimens (Group RF), the effect of the compressive contribution of the GFRP bars when determining the P-M interaction diagram was investigated. A total of two theoretical diagrams were drawn with the first including the compressive contribution of the GFRP bars by assuming the modulus in compression is equal to the modulus in tension (i.e. $E_{fc} = E_{ft}$), as shown in Figure 10a, whereas the second ignored the compressive contribution of the bars (i.e. $E_{fc} = 0$), as shown in Figure 10b.

When taking into account the compressive contribution of the GFRP bars the experimental result of the concentrically loaded and 50 mm eccentrically loaded specimens (RF-0 and RF-50) yielded values above the theoretical P-M diagram using the small strips method with comparable results, as shown in Figure 10a. However, the data point of the 25 mm eccentrically loaded specimen fell below the theoretical P-M diagram developed by the small strips method. Errors in testing may be the reason for the low experimental results. This can be seen in the load versus axial deformation curves for the four groups of specimens loaded in 25 mm eccentricity, as shown in Figure 13. The initial slope of the load-displacement curve of Specimen RF-25 was lower than that of the other specimens. This could be due to errors in aligning the specimen resulting in load not being applied exactly at 25 mm eccentricity [11]. Furthermore, the failure location of the internal reinforcement of this specimen was located at the top of the specimen rather than at mid-height [11]. On the other hand, the experimental results of the eccentrically loaded specimens yielded values below the theoretical P-M diagram using the conventional rectangular stress block method. Therefore, when taking into account the compressive contribution of the GFRP bars, the small strips method provided a more accurate approximation of the experimental loads and bending moment capacities for Group RF specimens for the different types of loading as compared to the conventional rectangular stress block method.

When ignoring the compressive contribution of the GFRP bars, the axial load capacity in pure compression is decreased as the second part Eq. (14) is reduced to 0 (E_{fc} = 0) providing a conservative approach for the concentric loading condition. It should be noted that similar to Specimen RF-25, Specimen RF-50 also failed at the top of the specimen rather than in the instrumented region as discussed in [11]. Having said this, the 50 mm eccentrically loaded column shows good agreement with the interaction diagram for this case with the experimental data point above the theoretical diagram for the two methods. However, the 25

535 mm eccentrically loaded column falls below the rectangular stress block method diagram but
536 shows relatively good agreement with the small strips method, although the experimental
537 load capacity value is 3.4% lower than that obtained theoretically using the small strips
538 method. As mentioned above errors in testing of this column did occur. In general,
539 considering that the compressive properties of FRP bars has not been extensively understood,
540 especially when embedded in concrete, it is safer to say that ignoring the compressive
541 contribution of the GFRP bars and drawing the theoretical P-M diagram based on the small
542 strips method is the most accurate and safe alternative for the design of such columns at this
543 stage. Having said this, for the small strips method further consideration of the maximum
544 stress limited to the concretes stress-strain curve to allow for differences between the cylinder
545 strength and in-place column specimen strengths, which may vary between $0.85f_c$ to $0.9f_c$, as
546 well as each specimen's strength at the respective day of testing should be taken into account
547 when drawing the P-M diagrams as explained below with the conclusions slightly varying.

548 Considering that the theoretical P-M diagrams were drawn based on the concrete compressive
549 strength at the first day of testing and knowing that the strength of concrete is ever increasing,
550 a discussion of the effects of this is necessary. The concentric specimens were tested first,
551 followed by the 25 mm eccentrically loaded specimens than the 50 mm loaded specimens and
552 lastly the beam specimens. The concrete strength of each specimen tested on each day could
553 be determined based on a linear trend of the known concrete compressive strength
554 determined at each day tested. The increase in concrete strength for each specimen tested on a
555 different day will shift the theoretical P-M diagrams upwards, since the load and bending
556 moment capacity will increase. Therefore, the relationship between the experimental data
557 points as a comparison to these revised theoretical P-M diagrams should be taken into
558 account. In summary with the slight increase in concrete strength for each specimen, it was
559 realised that although the revised P-M diagrams would be shifted slightly upwards for both

560 methods, with the experimental data point of RF-50 now slightly below the P-M diagram for
561 the small strips method (when E_{fc}=E_{ft}) and rectangular stress block method (when E_{fc}=0), the
562 same outcomes and conclusions stated above for Group RS and RF specimens were
563 acceptable. Therefore, the small strips method for predicting the P-M interaction relationship
564 was a more safe and accurate approach as compared to the rectangular stress block method.
565 Furthermore, ignoring the compressive contribution of the GFRP bars is also the best method
566 for those specimens.

567 Furthermore, it should be noted that the Australian standard AS3600 – 2009 [20] mentions
568 that if a stress-strain relationship is used for concrete, the maximum stress of the concrete
569 shall be modified to $0.9f_c$. In the standard the parameter f_c denotes the characteristic
570 compressive cylinder strength of concrete at 28 days (f_c'), but in this study f_c will be
571 represented as the concrete strength at the first day of testing, as mentioned above. In this
572 study the maximum stress was limited to $0.85f_c$ as explained in Section 4.1 to take into
573 account size and shape effects between the cylinders and column specimens. If the maximum
574 stress is modified to $0.9f_c$ the P-M diagram for the specimens of Group RS and RF developed
575 using the small strips method will shift upwards to just slightly under the diagram developed
576 using the rectangular stress block method, as shown in Figure 14. However, in terms of the
577 Group RF specimens, the experimental data points are more matched or appropriate at this
578 stage with the level of knowledge on GFRP reinforced columns to the values obtained by the
579 small strips method using a maximum stress of $0.85f_c$ rather than those obtained by the
580 rectangular stress block method, as explained above and shown in Figure 10 and Figure 14.
581 Most notably, when utilising the small strips method with a maximum stress of $0.9f_c$ and
582 assuming E_c = 0 (Figure 14), the data point of Specimen RF-50 is above the P-M diagram
583 when using the concrete strength at the first day of testing but when using the concrete
584 strength at the day of testing the specimen (as explained above), the experimental load

585 capacity is just slightly lower than that of the theoretical value whereas the theoretical
586 moment capacity is similar to the experimental value. Therefore, for the GFRP reinforced
587 specimens it is recommended to limit the maximum concrete stress to $0.85f_c$ and neglect the
588 compressive contribution of the bars as a conservative approach for design. Having said this,
589 further experimental verification of the theoretical P-M diagrams is required for the GFRP
590 reinforced specimens.

591 On the other hand, for both the GFRP I-section and C-section encased specimens, the
592 developed theoretical models using the small strips method utilising a maximum stress of
593 $0.85f_c$ yielded results that were conservative as compared to the experimental results, as
594 shown in Figures 11 and 12. This may be due to the assumption of using only the flanges of
595 the sections for the determination of the forces. If the contributions of the webs of these
596 sections are taken into account, the theoretical load and moment interaction diagram will shift
597 upwards. Having said this, considering the limited studies and the orthotropic nature of the
598 GFRP pultruded material as well as the high dispersion in compressive properties it is safer to
599 have a higher factor of safety for the members encased with such materials. Further research
600 is required to fully develop and understand the P-M interaction diagrams of these specimens.
601 It is interesting to note that although Specimen C-B showed signs of a typical shear failure
602 and was not plotted in Figure 12, the experimental bending moment capacity of this specimen
603 was well above the theoretical prediction. In fact, the experimental bending moment of 43.4
604 kN.m was approximately 46% higher than that obtained by the theoretical approach.

605 It should be noted that the strains in tension and compression in the GFRP bars and GFRP
606 sections for all the points along the interaction diagram were checked in terms of the ultimate
607 strains even when the compressive contribution of the GFRP bars were neglected. No failure
608 in these bars or flanges of the sections occurred when the strain in concrete reached its
609 ultimate value of 0.003. The compressive ultimate strain of the GFRP bars was calculated by

610 assuming the compressive modulus was equal to the tension modulus and the compressive
611 strength was equal to 50% of the tensile strength as reported by Deitz et al. [26]. It should be
612 noted that as mentioned above in the preliminary testing of the GFRP sections, potential
613 premature failure may have occurred for these sections when tested in compression due to
614 local end crushing, local end brooming, or geometric instabilities. This premature failure will
615 result in a lower rupture strain and compressive strength obtained but will not affect the
616 compressive modulus, which is determined as the initial slope of the stress and strain curves.
617 In drawing the P-M interaction diagram, the theoretical strain in compression was checked
618 against the rupture strain obtained from the compression testing and it was found that at the
619 first peak load no failure of the flanges of the sections occurred. Further investigation into the
620 compressive properties of these materials is required before they can be properly used in
621 design and construction.

622 As an extension, the strain data obtained from the steel and GFRP reinforcement in
623 compression and tensile were used to determine the experimental neutral axis for the
624 specimens loaded in 25 and 50 mm eccentricity, which led to calculating the load and
625 bending moment capacities. This was done by assuming linear strain distribution and by
626 calculating the concrete response using the small strips method. Furthermore, only Specimens
627 RS and RF were investigated since the assumption of neglecting the contribution of the webs
628 of the GFRP encased specimens would not provide a good comparison with the experimental
629 values. Table 5 shows the comparison of the capacities by three methods; obtained
630 experimentally, by the small strips method utilising a maximum concrete stress of $0.85f_c$ and
631 assuming concrete has reached ultimate strain of 0.003 as explained above and by using the
632 strain gauge data. Unfortunately, the strain reading of the GFRP bar in compression for
633 Specimen RF-25 was lost and therefore it was assumed to be equal to the value obtained for
634 Specimen RS-25 of 0.374%. It can be seen that good correlation in the capacities obtained by

635 the three methods was obtained for Specimens RS-50 and RF-50 when assuming the
636 compressive modulus is equal to zero. However, when assuming the compressive and tensile
637 moduli are equal for Specimen RF-50, the moment capacity obtained by the strain gauge data
638 is 4% higher than that obtained experimentally. On the other hand, there was not a good
639 correlation in the capacities for Specimens RS-25 and RF-25, with the moment capacities
640 calculated using the strain gauge data much higher than those obtained experimentally, while
641 the load capacities also varied considerably, as shown in Table 5. This was also the case for
642 Specimens I-25 and C-25. This would question the accuracy of the strain gauge data for the
643 tensile reinforcement in the 25 mm eccentrically loaded specimens which may be prone to
644 sensitivity issues with the bars subjected to small values of compressive and tensile strains
645 close to the maximum load. Furthermore, as mentioned above only one strain gauge was
646 placed on the tension and compression longitudinal bars and sections and no average could be
647 obtained for each value. Also un-warranted premature stressing of the bars from the pouring
648 of concrete and curing could cause some issues. It should be noted similar conclusions were
649 drawn when the rectangular stress block method was utilized in conjunction with the strain
650 gauge data to obtain the capacities when compared with the theoretical values obtained by the
651 same method along with the experimental values.

652 **6.0 Parametric Study**

653 The analytical model was used to study the effects of two main parameters on the structural
654 performance of GFRP reinforced square concrete columns in terms of the interaction
655 diagrams. The parameters studied are: (a) concrete compressive strength (f_{co}), and (b)
656 longitudinal GFRP reinforcement ratio. Only the small strips method utilising a maximum
657 stress of $0.85f_c$ was implemented to draw the P-M interaction diagrams in this parametric
658 study and the compressive contribution of the GFRP bars was neglected.

The cross-section dimensions and the material properties of the columns studied were the same as that used in the experimental testing. The columns were square in cross-section with a side width of 210 mm. In addition, while the effect of each parameter was investigated, all other parameters were kept constant. Therefore, default values of each parameter were set when that parameter was not being used in the study. The following default values were set for each parameter: the compressive strength of concrete at the first day of testing (f_{co}) was 31 MPa; the longitudinal GFRP reinforcement ratio was 1.15%; and the ratio of the compressive modulus to the tensile modulus was 0 (E_{fc} = 0). Essentially these values were the same as those of the experimentally tested specimens.

6.1. Influence of Concrete Strength, f_{co}

Depending on the quality control that is implemented, variations in concrete strengths most likely occur. Therefore, it is important to study the effects of varying the concrete compressive strength on the structural behaviour of GFRP reinforced concrete columns. A total of four concrete strengths were studied as follows: 31, 40, 50 and 60 MPa. The P-M strength interaction diagram for all the different cases is shown in Figure 15. It should be noted that the formula for the Young's modulus of concrete also varies for strengths over 40 MPa. As expected, as the concrete strength increases, so does the load and bending moment capacities. The strains in the tension and compression bars for all the points along the interaction diagram were checked in terms of the ultimate strains for each case and no failure in these bars occurred for all concrete strengths when the strain in concrete reached its ultimate value. In fact, as the concrete strength increased, the strains in the tensile bars at the ultimate bending condition (P = 0 kN) increased, but remained below the ultimate value. It was seen that a tensile strain of 1.4% was obtained at the ultimate bending condition when the concrete strength at the first day of testing was 60 MPa which is lower than the ultimate value of 2.41%.

6.2. Influence of longitudinal GFRP reinforcement ratio

A total of four longitudinal GFRP reinforcement ratios were studied as follows: 1.15, 3, 5 and 7%. The P-M strength interaction diagram for the different reinforcement ratios when neglecting the compressive contribution of the GFRP bars ($E_{fc} = 0$) is shown in Figure 16a. It can be seen that as the reinforcement ratio increases, the axial load capacities for pure compression decreases slightly because the modulus in compression is reduced to zero and the second part of Eq. (14) becomes also zero. Furthermore, as the reinforcement ratios increases, the bending moment capacity at lower levels of load capacity increases.

It is interesting to see the behaviour of the P-M interaction diagram when taking into account the compressive contribution of the GFRP bars ($E_{fc} = E_{ft}$) as shown in Figure 16b. Most notably, to calculate the axial capacity for pure compression the second part of Eq. (14) is taken into account unlike that when $E_{fc} = 0$. As a result, for this case as the reinforcement ratio increases so does the axial capacity for pure compression. On the other hand similar to Figure 16a, as the reinforcement ratio increases the bending moment capacity at lower levels of load capacity increases. Therefore, as reported by Choo et al. [3] the P-M interaction diagrams of GFRP reinforced columns do not experience any balanced points, unlike that of steel reinforced columns.

Furthermore, for all the cases no failure occurred for the GFRP bars in tension or compression when the concrete reached the ultimate strain. In fact, as the reinforcement ratio increased, the strains in the tensile bars at the ultimate bending condition (P = 0 kN) decreased.

7.0 Conclusions

Based on the experimental results and the analytical analysis of this study it can be concluded that concrete columns reinforced with GFRP bars and encased with pultruded GFRP sections

708 can be potentially analysed using the same procedure used for conventional steel reinforced
709 concrete columns. The small strips method adopted in this study for predicting the P-M
710 interaction relationship provided more accurate results as compared to the rectangular stress
711 block method for the GFRP reinforced specimens. Furthermore, considering that the
712 compressive properties of FRP bars has not been extensively understood, especially when
713 embedded in concrete, it is safer to say that ignoring the compressive contribution of the
714 GFRP bars and drawing the theoretical P-M diagram based on the small strips method is the
715 most accurate and safe alternative for the design of such columns at this stage. Further
716 experimental verification of the theoretical P-M diagrams is required for the GFRP reinforced
717 specimens considering the limited number of specimens in this study, the value of the
718 maximum stress on the stress-strain diagram for concrete (varies between $0.85f_c$ to $0.90f_c$)
719 and the strength of each specimen on the respective day of testing.

720 In terms of the GFRP encased specimens, the small strips method provided satisfactory and
721 conservative estimates of the maximum load and bending moment capacities. It was found
722 that the most accurate estimate of the maximum axial capacity for the GFRP reinforced
723 specimen under concentric loading was achieved when taking into account the compressive
724 contribution of the GFRP bars based on the elastic theory and assuming the strain in the bars
725 is equal to the concretes ultimate compressive strain. Furthermore, in terms of the GFRP
726 pultruded sections, a high dispersion in the compressive properties of these types of materials
727 will require better testing procedures to prevent premature failures, better quality control at
728 the manufacturing level, and further investigation into the compressive properties of these
729 materials before they can be properly used in design and construction. In addition, the
730 experimental results of the GFRP reinforced and GFRP encased beam specimens could not
731 be compared to the theoretical models and further research elaboration is necessary to
732 investigate this along with the P-M diagrams of GFRP encased specimens.

733 Based on the parametric study, the load and bending moment capacities increase with the
734 increase in concrete strength. Furthermore, the interaction diagrams of GFRP reinforced
735 columns do not experience balanced points unlike that of steel reinforced columns. This study
736 is believed to give an understanding on the behaviour of GFRP reinforced and GFRP encased
737 concrete columns subjected to various loading conditions.

738 **Acknowledgments**

739 The authors would like to acknowledge the technical assistance of Messrs Alan Grant,
740 Fernando Escribano, Richard Gasser, Cameron Neilson, Duncan Best and Ritchie McLean.
741 The contribution of Ms. Philippa Langford is greatly appreciated. The first author would like
742 to thank the University of Wollongong, Australia for the support of his Ph.D. scholarship.

743 **References**

744 [1] ACI 440.1R – 15, Guide for the Design and Construction of Structural Concrete
745 Reinforced with Fiber-Reinforced Polymer (FRP) Bars, American Concrete Institure,
746 Farmington Hills, MI, 2015

747 [2] N. Kawaguchi, Ultimate Strength and Deformation Characteristics of Concrete Members
748 Reinforced with AFRP Rods under Combined Axial Tension or Compression and Bending,
749 Fiber-Reinforced-Plastic Reinforcement for Concrete Structures, SP-138, A, (1993).

750 [3] C.C. Choo, I.E. Harik, H. Gesund, Strength of Rectangular Concrete Columns Reinforced
751 with Fiber-Reinforced Polymer Bars, ACI Structural Journal, 103 (3) (2006a) 452 – 459.

752 [4] C.C. Choo, I.E. Harik, H. Gesund, Minimum reinforcement ratio for fiber-reinforced
753 polymer reinforced concrete rectangular columns, ACI Structural Journal, 103 (3) (2006b)
754 460 – 466.

755 [5] H.J. Zadeh, A. Nanni, Design of RC columns using glass FRP reinforcement, Journal of
756 Composites for Constructions, 17(3) (2013) 294 – 304.

757 [6] M.N.S. Hadi, H. Karim, M.N. Sheikh, Experimental Investigations on Circular Concrete
758 Columns Reinforced with GFRP Bars and Helices under Different Loading Conditions,
759 Journal of Composites for Construction, 10.1061/(ASCE)CC.1943-5614.0000670 (2015)

760 [7] J. Tomblin, E. Barbero, Local buckling experiments on FRP columns, Thin-Walled
761 Structures, 18(2) (1994) 97-116.

762 [8] A. Zureick, D. Scott, Short-term behaviour and design of fiber-reinforced polymeric
763 slender members under axial compression, 1(4) (1997) 140 – 149.

764 [9] J.R. Correia, F.A. Branco, J. Ferreira, GFRP–concrete hybrid cross-sections for floors of
765 buildings, Engineering Structures, 31(6) (2009) 1331-1343.

766 [10] W.H. Kwan, M. Ramli, Indicative performance of fiber reinforced polymer (FRP)
767 encased beam in flexure, Construction and Building Materials, 48(0) (2013) 780-788.

768 [11] M.N.S Hadi, J. Youssef, Experimental Investigation of GFRP Reinforced and GFRP
769 Encased Square Concrete Specimens under Axial and Eccentric Load, and Four-Point
770 Bending Test, Journal of Composites for Construction, 10.1061/(ASCE)CC.1943-
771 5614.0000675, (2016).

772 [12] AS1391-2007, Metallic materials – Tensile testing at ambient temperatures, Standards
773 Australia, Sydney, Australia, 2007

774 [13] Pultrall, Inc. (2012). V-ROD - Specification HM, Thetford Mines, Canada,
775 www.pultrall.com

776 [14] ASTM D7205-11, Standard test method for tensile properties of fiber reinforced
777 polymer matrix composite bars, American Society for Testing and Materials, West
778 Conshocken, PA, USA, 2011

779 [15] GRP (Glass Reinforced Products) (2008), Load Test of Pultruded Sections – Report
780 Data, Lytton, Queensland, Australia (www.grpaustralia.com.au), accessed Aug. 08, 2014.

781 [16] ISO. 527-4, Determination of tensile properties of plastics. Part 4: Test conditions for
782 isotropic and orthotropic fiber-reinforced plastic composites, *ISO*, European Committee for
783 Standardisation, Brussels, Belgium, 1997

784 [17] ASTM D695-15, Standard test method for compressive properties of rigid plastics,
785 American Society for Testing and Materials, West Conshohocken, PA, 2015.

786 [18] E.J. Barbero, S. Makkapati, J.S. Tomblin, Experimental determination of the
787 compressive strength of pultruded structural shapes, Composites Science and Technology,
788 59(13) (1999) 2047 – 2054.

789 [19] K.H. Yang, J.H. Mun, M.S. Cho, T.H.K. Kang, (2014), Stress-Strain Model for Various
790 Unconfined Concretes in Compression, ACI Structural Journal, 111 (4) (2014) 819 – 826.

791 [20] AS3600-2009, Concrete Structures, AS3600-2009, Standards Australia, Sydney,
792 Australia, 2009

793 [21] P.K. Mallick, Fiber Reinforced Composites, Material, Manufacturing, and Design,
794 Marcell Dekker, Inc., New York, 1998, 469pp.

795 [22] W.P. Wu, Thermomechanical Properties of Fiber Reinforced Plastic (FRP) Bars, PhD
796 dissertation, West Virginia University, Morgantown, WV,1990. 292 pp.

797 [23] M.R. Ehsani, Glass-Fiber Reinforcing Bars, Alternative Materials for the Reinforcement
798 and Prestressing of Concrete, J.L. Clarke, Blackie Academic & Professional, London, UK,
799 1993, pp. 35 – 54.

800 [24] O. Chaallal, B. Benmokrane, Physical and Mechanical Performance of an Innovative
801 Glass-fiber-reinforced Plastic Rod for Concrete and Grouted Anchorage, Canadian Journal of
802 Civil Engineering, 20 (2) (1993) 254-268.

803 [25] K. Kobayashi, T. Fujisaki, Compressive behaviour of FRP reinforcement in non-
804 prestressed concrete members, 2nd International RILEM Symposium on Non-Metallic (FRP)
805 Reinforcement for Concrete Structure*s*, E & FN Spon, London, 267–274, 1995

806 [26] D.H. Deitz, I. E. Harik, H. Gesund, Physical properties of glass fiber reinforced polymer
807 rebars in compression, Journal of Composites for Construction, 7(4) (2003) 363 – 366.

808 [27] ACI 318-14, Building code requirements for structural concrete, American Concrete
809 Institute, Farmington Hills, MI, 2014.

810 [28] CSA S806-12, Design and Construction of Building Structures with Fiber-Reinforced
811 Polymers, Canadian Standards Association, Toronto, Canada, 2012

812 [29] H. Tobbi, A.S. Farghaly, B. Benmokrane, Concrete Columns Reinforced Longitudinally
813 and Transversally with Glass Fiber-Reinforced Polymer Bars, ACI Structural Journal, 109(4)
814 (2012) 551-558.

815 [30] H. Tobbi, A.S. Farghaly, B. Benmokrane, Behaviour of Concentrically Loaded Fiber-
816 Reinforced Polymer Reinforced Concrete Columns with Varying Reinforcement Types and
817 Ratios, ACI Structural Journal, 111(2) (2014) 375-386.

818 [31] V. Yazici, M.N.S Hadi, Axial Load-Bending Moment Diagrams of Carbon FRP
819 Wrapped Hollow Core Reinforced Concrete Columns, Journal of Composites for
820 Constructions, 13(4) (2009) 262 – 268.

821

List of Figures

Fig. 16. Influence of longitudinal GFRP reinforcement ratio on P-M interaction diagrams: (a) Compressive contribution of GFRP bars ignored ($E_{fc} = 0$); and (b) Compressive contribution of GFRP bars included ($E_{fc} = E_{ft}$)

852 **List of Tables**

853

861

862 **Table 1.** Tensile and compressive properties of the GFRP pultruded structural sections

863 (averages and sample standard deviations)

Property	I-section Longitudinal			C-section Longitudinal
	WEB	FLANGE	GLOBAL[a]	WEB
Tensile Strength (MPa)	386.5 ± 17.4	430.2 ± 32.7	405.9 ± 32.91	318.1 ± 31.8
Tensile Modulus (GPa)	20.7 ± 0.7	26.0 ± 2.2	23.4 ± 3.2	27.1 ± 2.1
Tensile Rupture Strain (%)	1.89 ± 0.12	1.70 ± 0.23	1.80 ± 0.19	1.22 ± 0.10
Compressive Strength (MPa)	201.3 ± 28.9	221.4 ± 34.3	211.6 ± 32.9	275.4 ± 74.1
Compressive Modulus (GPa)	21.6 ± 2.3	22.4 ± 2.3	22.0 ± 2.3	25.6 ± 2.7
Compressive Rupture Strain (%)	0.88 ± 0.11	0.91 ± 0.14	0.90 ± 0.12	0.96 ± 0.14

864 [a] The average results of all the coupons extracted from the flange and web of the I-section

865

866 **Table 2.** Experimental maximum load and bending moment capacity of specimens

Test Specimen	1st Maximum Load, P_{max} (kN)	Axial displacement at P_{max}, Δ (mm)	Lateral deflection at P_{max}, δ (mm)	Bending Moment, $M_{exp} = P_{max}(e + \delta)$ (kN.m)
RS-0	1350	2.87	0	0
RS-25	995	2.72	2.11	27.0
RS-50	747	2.65	2.66	39.3
RS-B	232	-	8.08[c]	27.3[d]
RF-0	1285	2.59	0	0
RF-25	803	3.00	2.21	21.9
RF-50	615	2.33	2.46	32.3
RF-B	340[a]	-	12.13[c]	40.0[d]
I-0	1425	3.13	0	0
I-25	1008	2.51	2.05	27.3
I-50	765	2.88	3.18	40.7
I-B	216[b]	-	13.47[c]	25.3[d]
C-0	1385	3.24	0	0
C-25	985	2.86	2.96	27.5
C-50	679	3.04	3.69	36.4
C-B	370	-	12.78[c]	43.4[d]

867 [a] The shear zones of only this specimen were wrapped with two layers of CFRP sheets.

868 [b] Failed prematurely by bearing. Data point could not be used on the P-M interaction diagram

869 [c] Midspan deflection of the beam specimens

870 [d] Calculated using Eq. (2).

871

872 **Table 3.** Experimental and theoretical axial capacity of Specimen RF-0

Experimental maximum axial load P_{max} (kN)	Theoretical, P_o (kN)			$\frac{P_{max}}{P_o}$		
	Eq. (12)	Eq. (13)	Eq. (14)	Eq. (12)	Eq. (13)	Eq. (14)
1285	1086	1440	1252	1.183	0.892	1.026

873

874 **Table 4.** Experimental and theoretical axial capacity of Specimen I-0 and C-0

Specimen	Experimental maximum axial load P_{max} (kN)	Theoretical P_o (kN) Eq. (14)	$\frac{P_{max}}{P_o}$
I-0	1425	1324	1.076
C-0	1385	1365	1.015

875

876

877 **Table 5.** Comparison of load and bending moment capacities for eccentrically loaded

878 specimens reinforced with bars

Specimen	Experimental		Theory – Small strips method[a]		Theory – Strain gauge data[b]		
	P (kN)	M (kN.m)	P (kN)	M (kN.m)	P (kN)	M (kN.m)	e (mm)
RS-25	995	27.0	980	24.5	887	31.1	35.1
RS-50	747	39.3	705	35.3	717	37.8	52.7
RF-25 ($E_c = E_t$)	803	21.9	884	22.1	713	31.9	44.7
RF-50 ($E_c = E_t$)	615	32.3	625	31.3	624	33.6	53.9
RF-25 ($E_c = 0$)	803	21.9	831	20.8	656	27.9	42.6
RF-50 ($E_c = 0$)	615	32.3	586	29.3	570	30.0	52.6

879 [a] Calculated by assuming concrete has reached ultimate compressive strain of 0.003 (refer to
880 Section 4.3)

881 [b] Calculated from the experimental strain gauge data and calculating the concrete response
882 using the small strips method

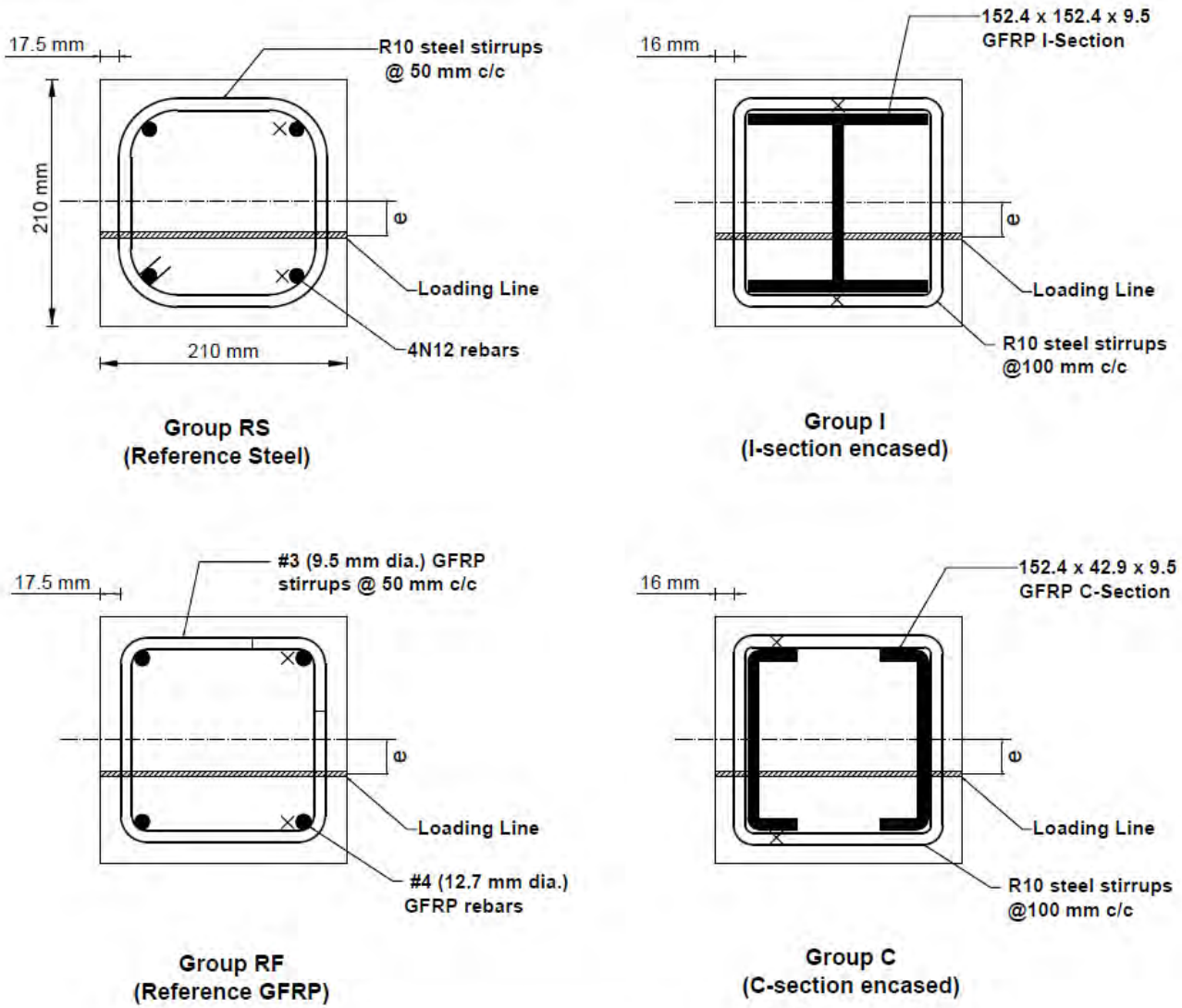

Fig. 1. Plan view of reinforcement details for all groups of specimens

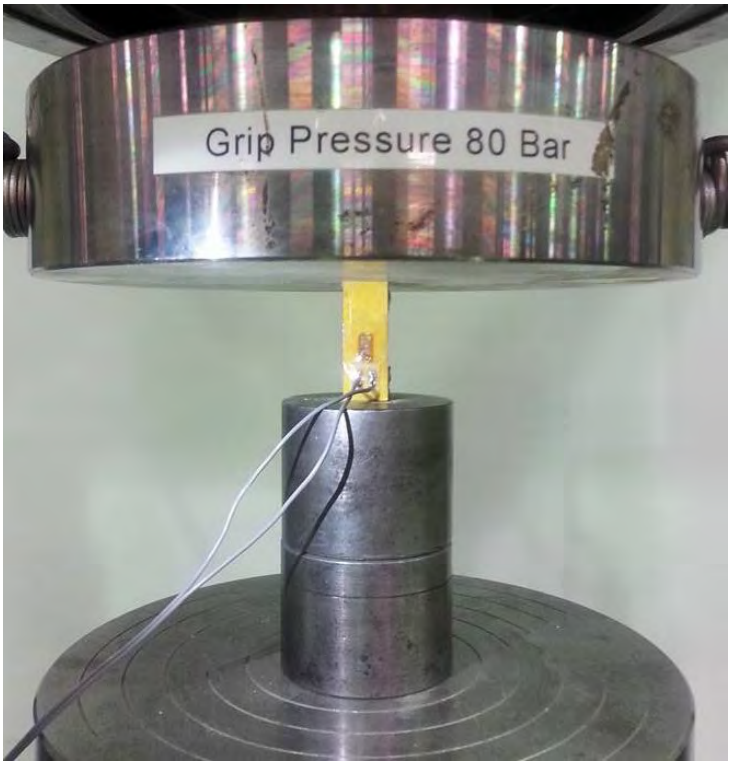

Fig. 2. Compression testing of pultruded GFRP sections

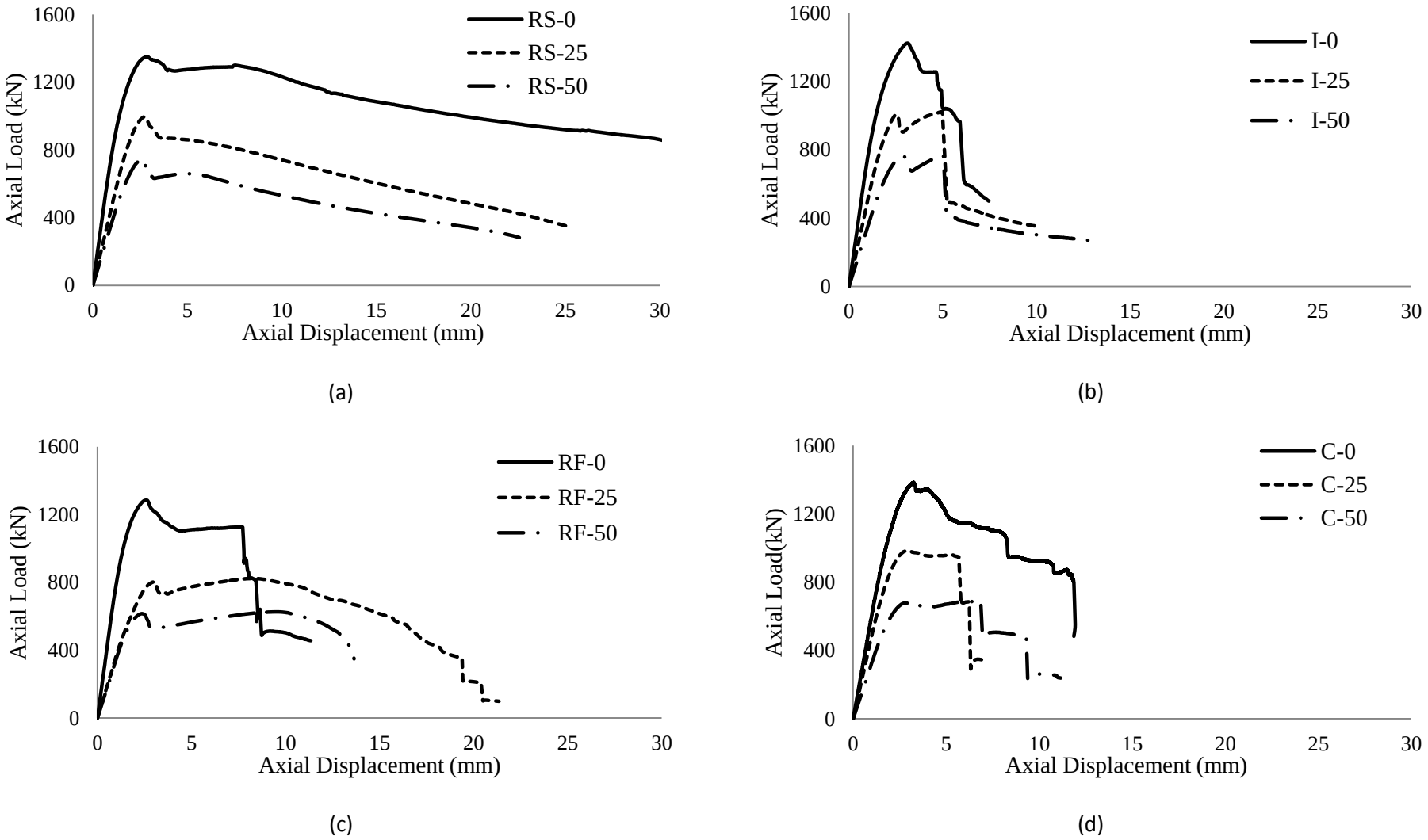

Fig. 3. Axial load-displacement relationships of column specimens with varying load eccentricities: (a) Group RS; (b) Group I; (c) Group RF; and (d) Group C

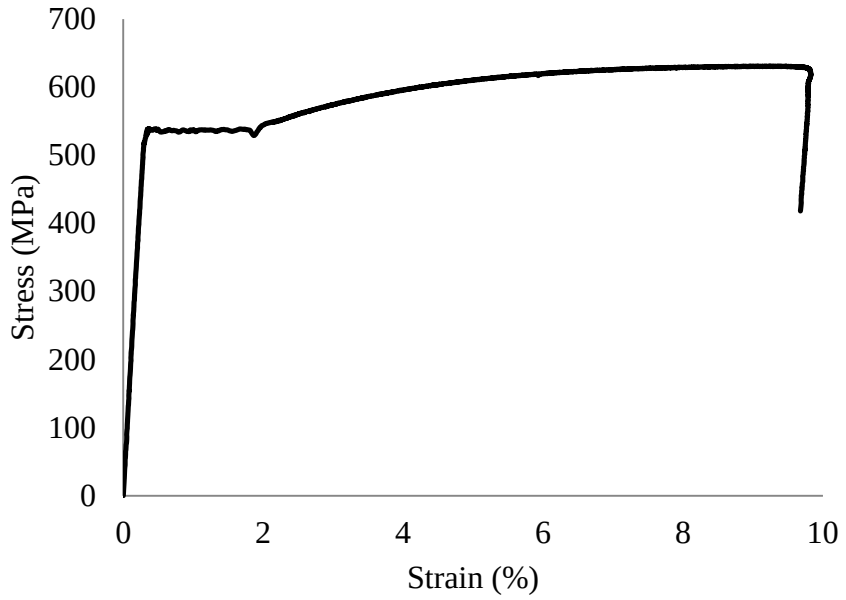

(a)

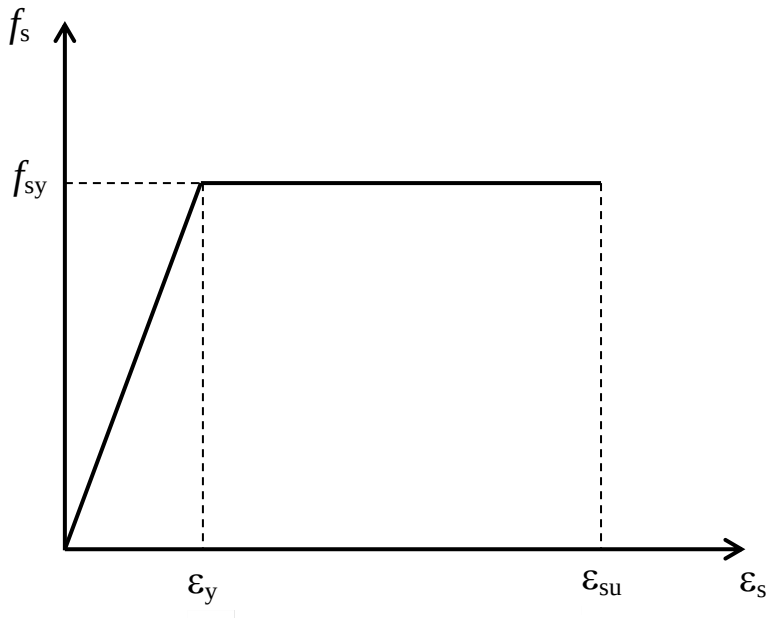

(b)

Fig. 4. Stress-Strain Relationships of N12 longitudinal steel bar:
(a) Experimental; and (b) Idealised

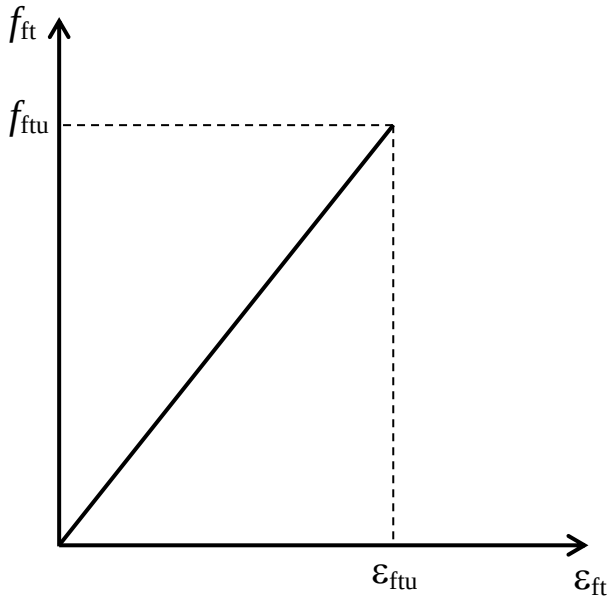

Fig. 5. Experimental and idealised stress-strain relationship of longitudinal GFRP bar

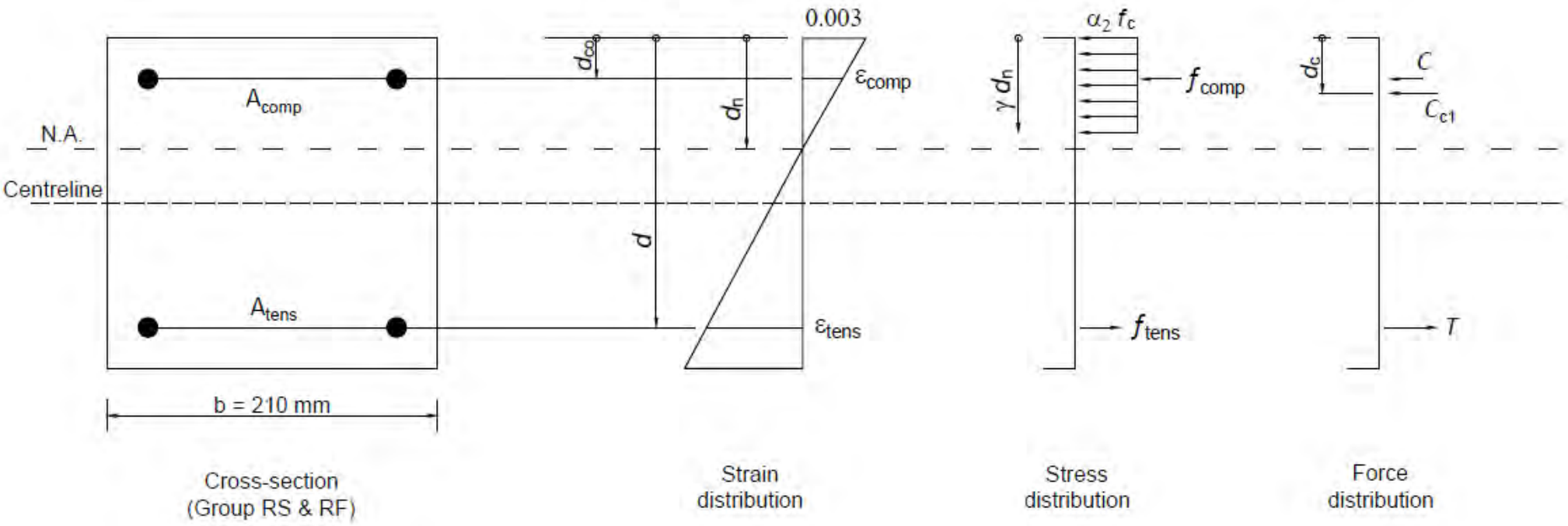

Fig. 6. Rectangular stress block method and force distribution of reinforcement for Group RS and RF specimens

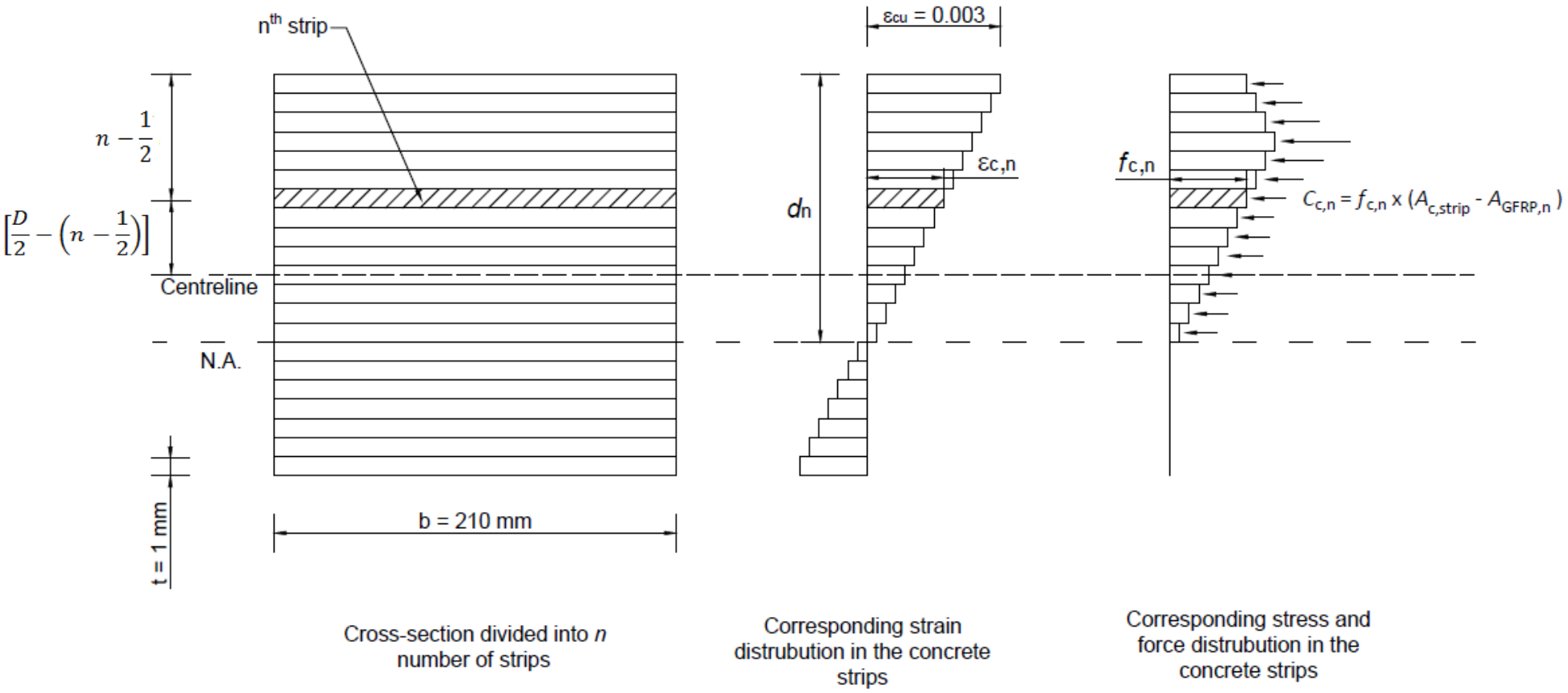

Fig. 7. Small strips method to determine the concrete compressive response

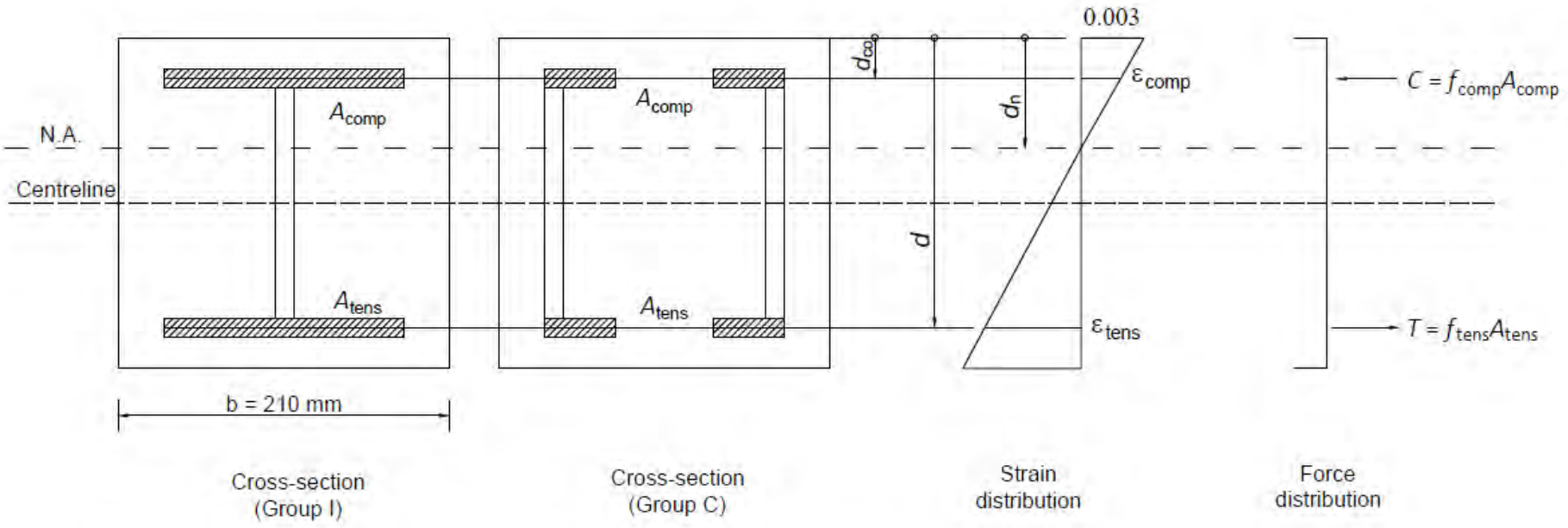

Notes: Concrete force distribution is calculated using the small strips method.
Force contribution of the webs is neglected.

Fig. 8. Force distribution of specimens of Group I and C

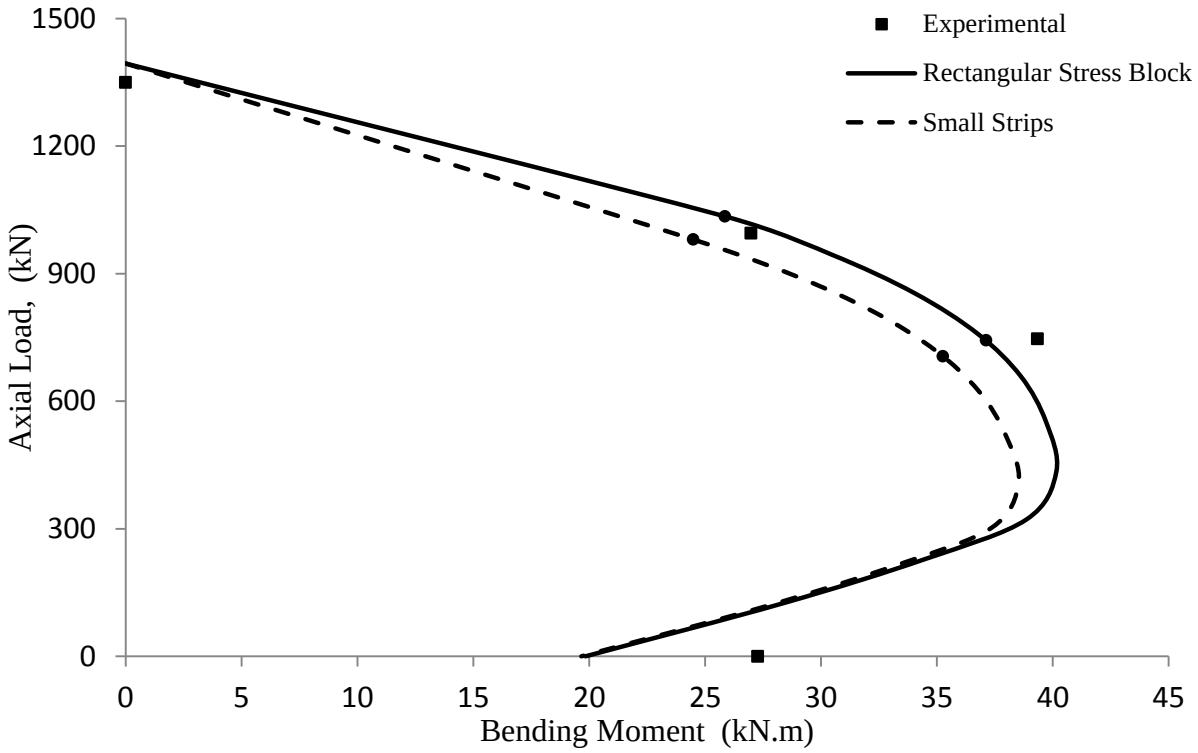

Fig. 9. Comparison of theoretical P-M diagrams and experimental results for Group RS specimens

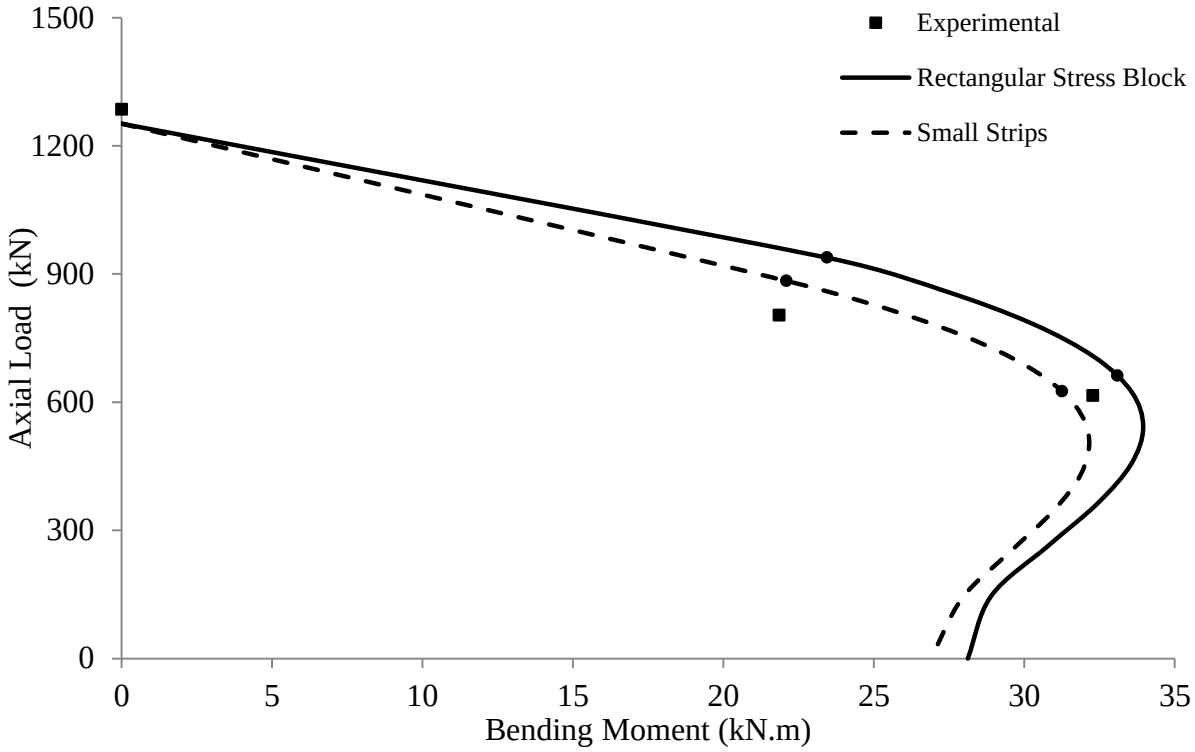

(a)

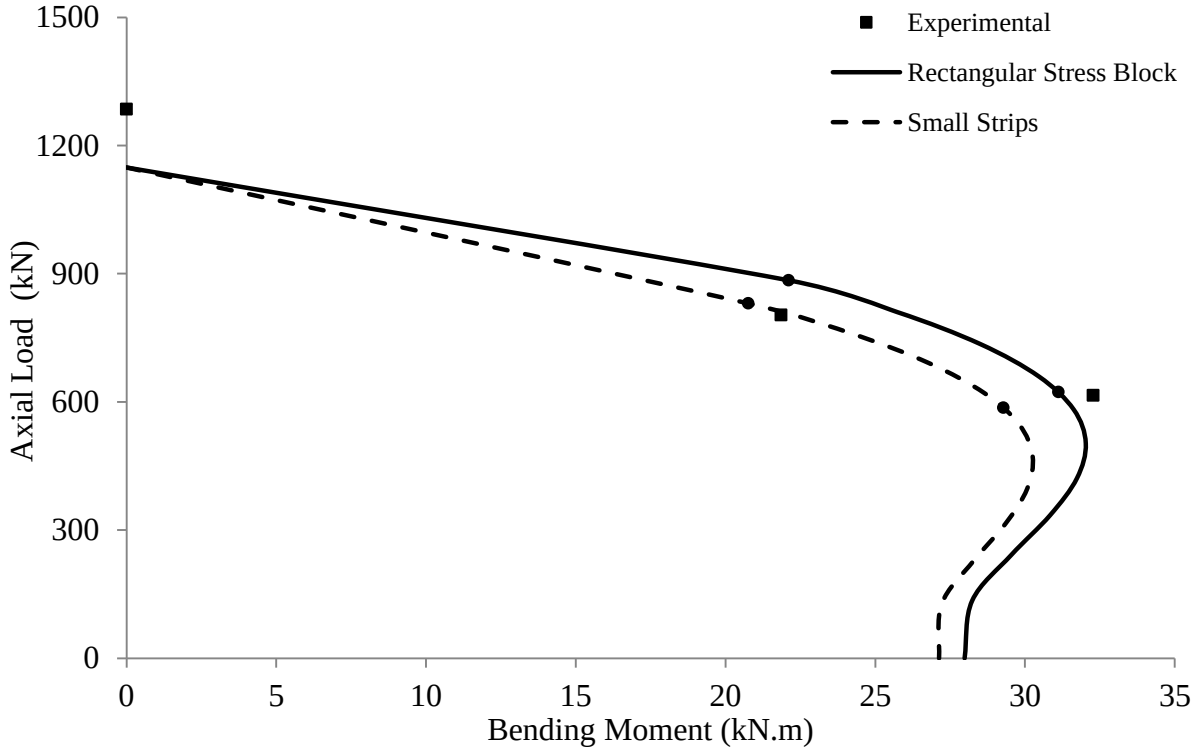

(b)

Fig. 10. Comparison of theoretical P-M diagrams and experimental results for Group RS specimens: (a) Compressive contribution of GFRP bars included ($E_{fc} = E_{ft}$); and (b) Compressive contribution of GFRP bars ignored ($E_{fc} = 0$)

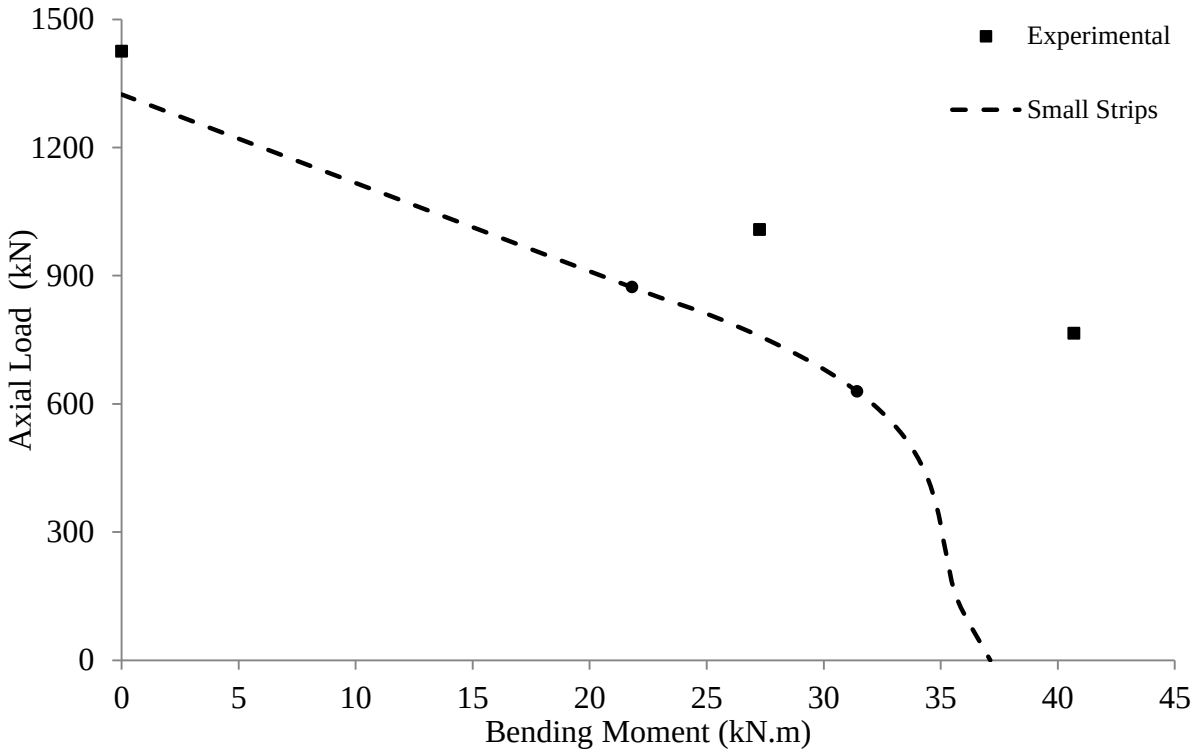

Fig. 11. Comparison of theoretical P-M diagrams and experimental results for Group I specimens

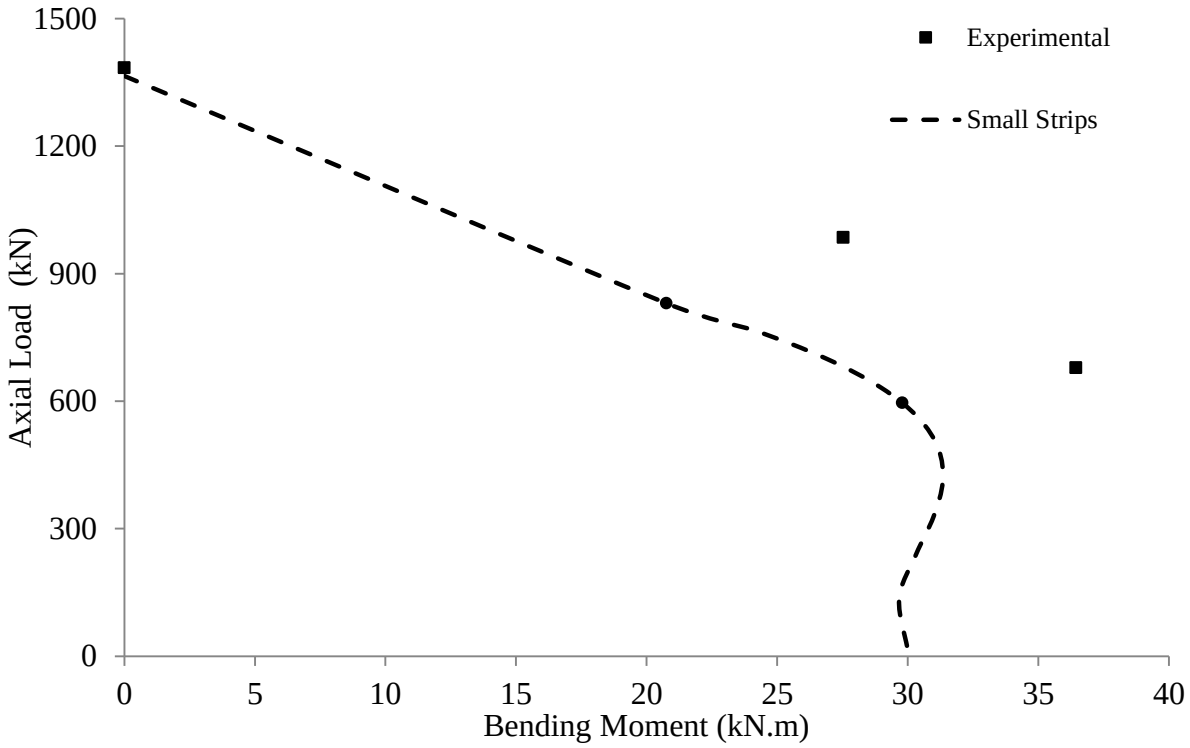

Fig. 12. Comparison of theoretical P-M diagrams and experimental results for Group C specimens

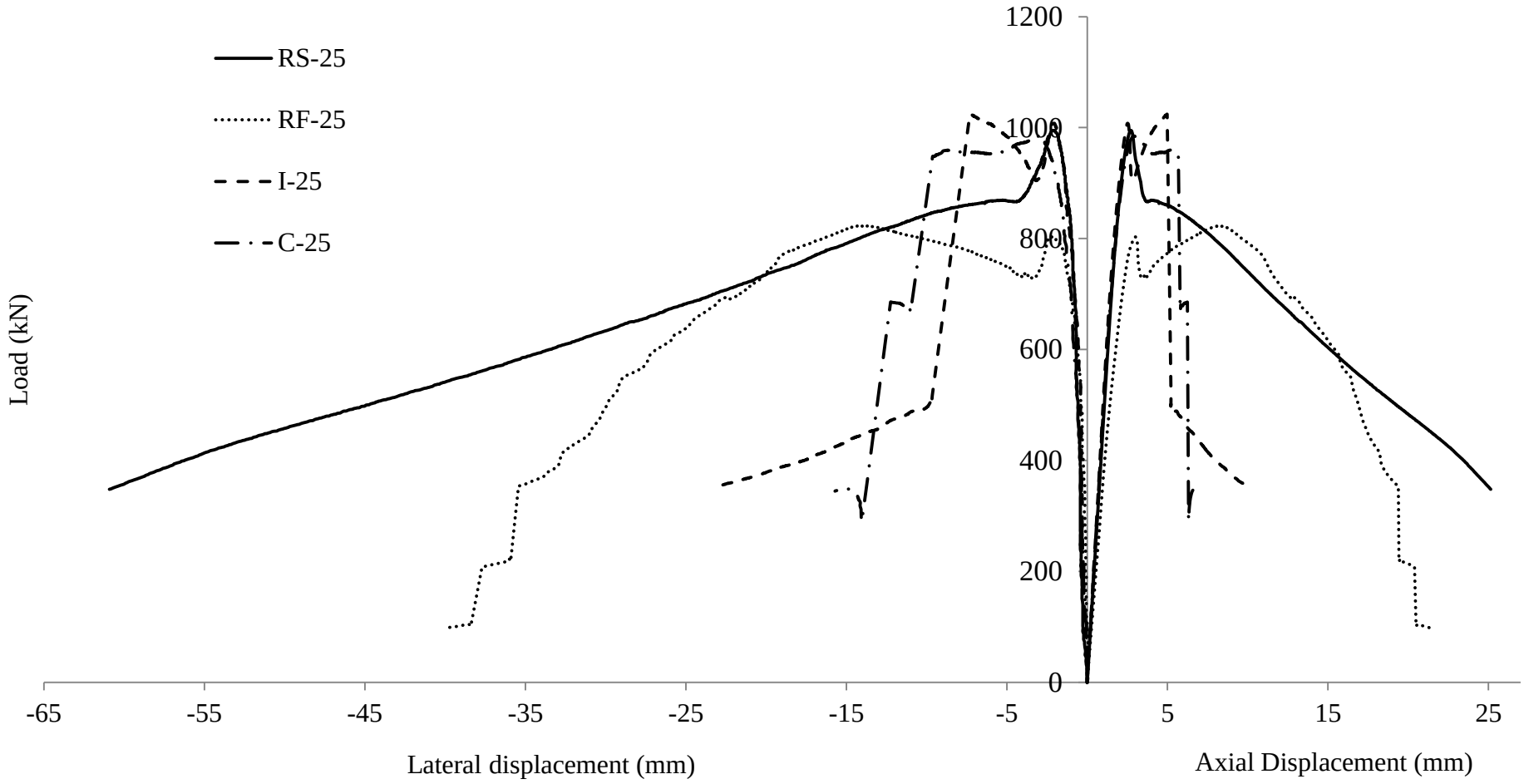

Fig. 13. Axial and lateral load-deflection curves of the 25 mm eccentrically loaded column specimens, e=25mm

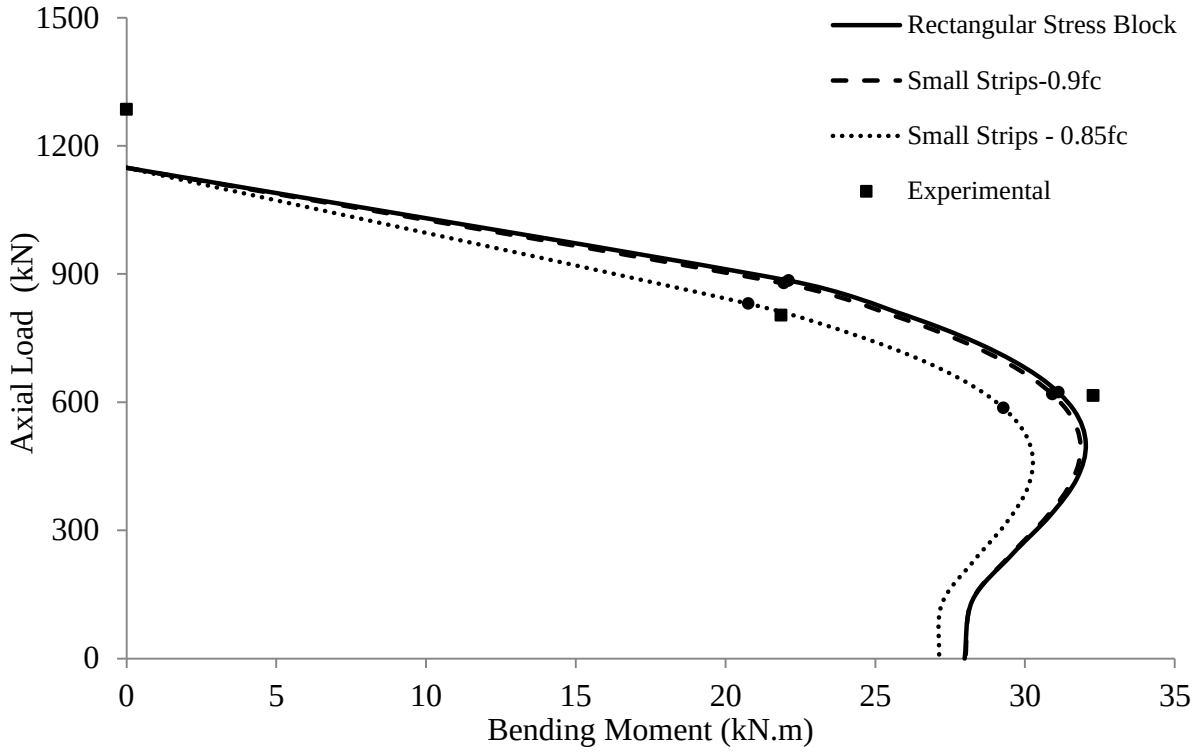

Fig. 14. Theoretical P-M diagrams of Group RF specimens when varying the maximum stress of concrete from $0.85f_c$ to $0.9f_c$ and assuming $E_{fc} = 0$

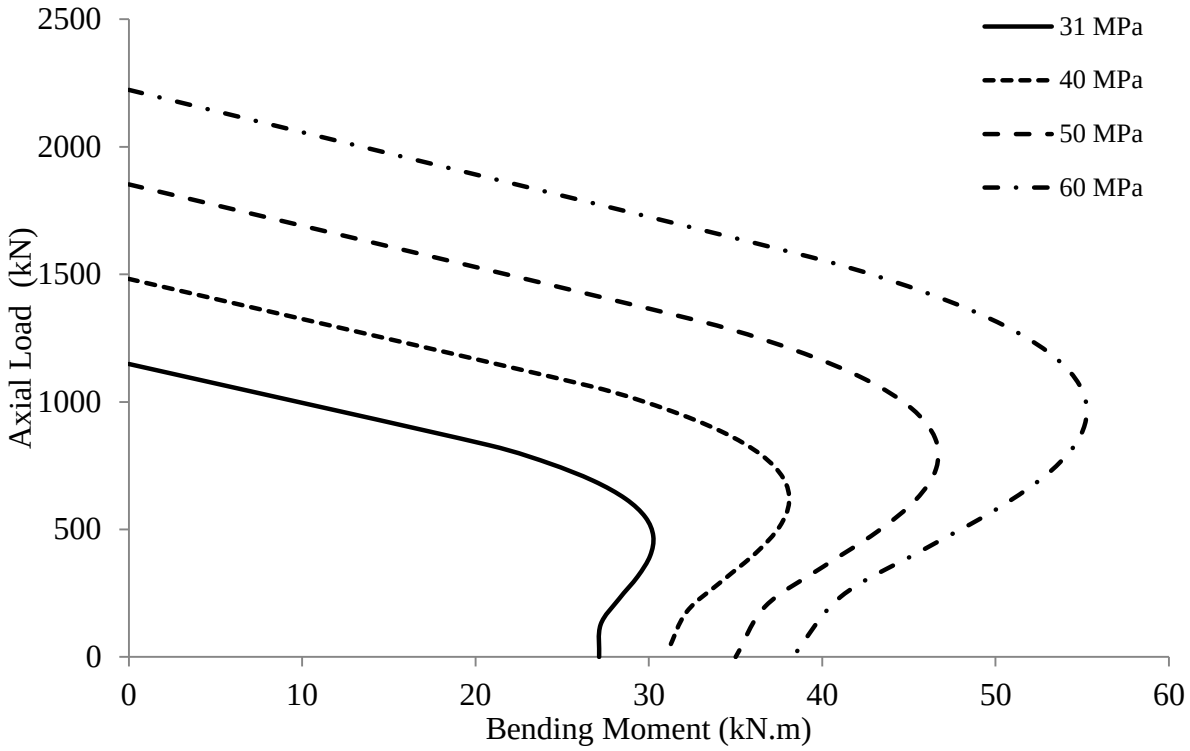

Fig. 15. Influence of concrete strength on P-M interaction diagrams for Specimens RF

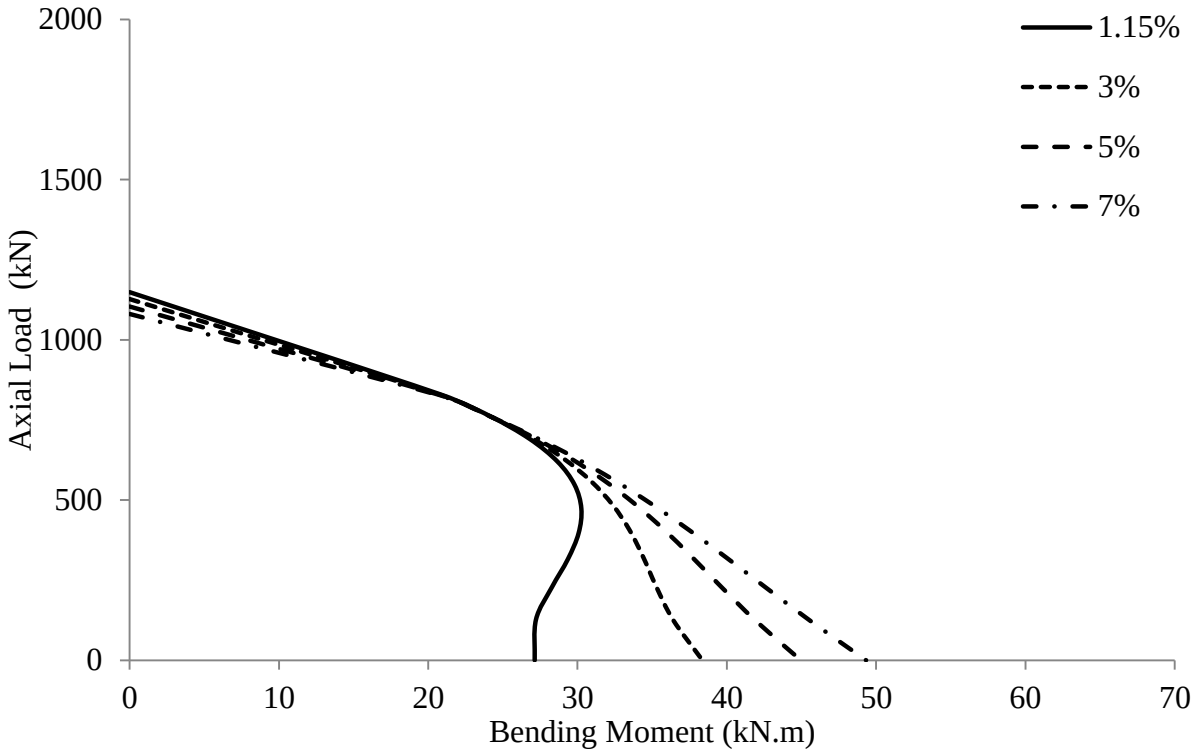

(a)

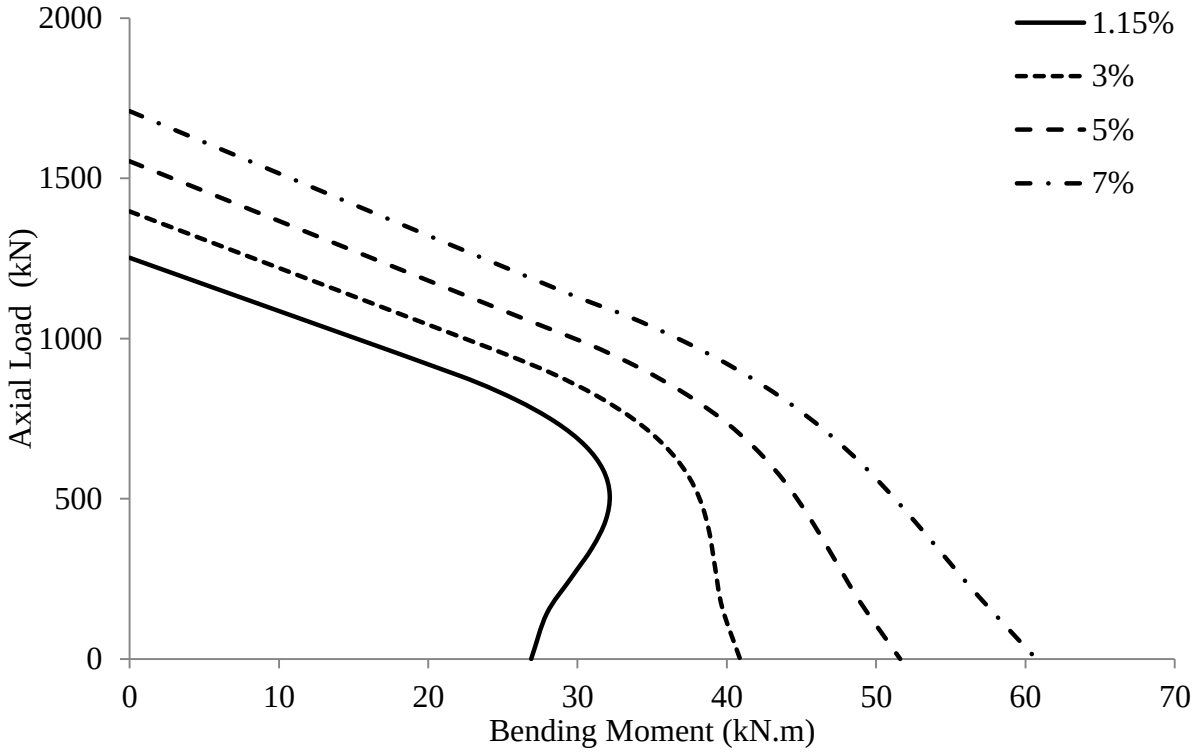

(b)

Fig. 16. Influence of longitudinal GFRP reinforcement ratio on P-M interaction diagrams: (a) Compressive contribution of GFRP bars ignored ($E_{fc} = 0$); and (b) Compressive contribution of GFRP bars included ($E_{fc} = E_{ft}$)